PETROLOGIC CONSTRAINTS OF CAMBRIAN MAFIC TO INTERMEDIATE VOLCANISM IN THE SOUTHERN OKLAHOMA AULACOGEN

by

JASPER HOBBS

B.A., BOSTON UNIVERSITY, 2013

A THESIS

submitted in partial fulfillment of the requirements for the degree

MASTER OF SCIENCE

Department of Geology
College of Arts and Sciences

KANSAS STATE UNIVERSITY
Manhattan, Kansas

2015

Approved by:

Major Professor
Matthew Brueseke

Abstract

The Southern Oklahoma Aulacogen (SOA) produced more than 250,000 km^3 of Cambrian mafic to silicic magmatism, associated with the opening of the Iapetus Ocean. In the Arbuckle Mountains, oil and gas exploration showed mafic to intermediate volcanic rock interbedded with rhyolite lavas. The first description of these lavas was a result of the 1982 drilling of the Hamilton Brothers Turner Falls well. Cuttings have been collected from this well and five others, and whole rock major and trace element analysis, Sr and Nd isotope analysis, and rare earth element analysis has been completed on these samples. These samples plot primarily as tholeiitic to transitional basalts to andesites. Trace element ratios show Zr/Nb values ranging from 8-10, K/Nb values ranging from 300-600, and Ba/Nb values ranging from 10-20, which overlap with known EM1 OIB values. Applying a conservative age of 535 Ma for these rocks yields $^{87}Sr/^{86}Sr_i$ values of 0.703970 to 0.706403 and epsilon Nd values of 1.67 to 3.22, which also fall within the accepted range of EMI values. $^{87}Sr/^{86}Sr_i$ increases with wt. % SiO_2 and K/P, consistent with the generation of evolved compositions via open-system processes. The sample with the least radiogenic Sr isotope ratio, combined with its trace element ratios is most consistent with an EM1-type source. These results, coupled with existing isotope and trace element constraints from regionally exposed dikes and plutonic rocks that crop out in the Wichita Mts., give better insight into understanding what tectonic model (lower-mantle derived hotspot or extension of the lithosphere) drove the magmatic production of the SOA. The results are more consistent with a lower-mantle origin for SOA mafic-intermediate magmatism, and indicate the potential for flood basalt volcanism.

Table of Contents

List of Figures

List of Tables

Acknowledgements

I would like to thank Dr. Matt Brueseke for all of your time and advice as an advisor, and for helping me become a better student and scientist. Thank you Dr. Kempton and Dr. Kirk for sitting on my committee and for your thoughtful edits. Thank you to Drs. Stan Mertzman, Doug Walker, and John Morton for their help with the analysis of my samples. Thank you to Bob Puckett and Casey Bulen for their help with locating the samples and for previous work in the area. I would like to thank Dr. Brenee King for being a great mentor and friend. Thanks to all of my friends in the geology department, especially Helder, Logan and Alyson for being my first friends at K-State, Tyler for the hockey talk, and Anna for all the comic relief. Thank you to Lindsey for being the best friend I could ask for. And last but not least, thank you to my family for always supporting me; I would not be where I am without you.

Chapter 1 - Introduction

The Southern Oklahoma aulocogen (SOA), which stretches through southern Oklahoma and into parts of Colorado and New Mexico (Fig. 1), has produced >250,000 km^3 of mafic-silicic magmatism. This magmatism can be related to the opening of the Iapetus Ocean during the late Precambrian and early Cambrian periods, likely due to the failed arm of a three-armed rift system due to the break up of the supercontinent Gondwanaland (Hanson et al., 2012). The SOA is believed to stretch at least 1,000 km from the Ouachita orogenic belt into the Laurentian craton with a width of 150 km and a depth of at least 8-12 km (Keller and Stephenson, 2007; Hanson et al., 2012). Initially, the extent of mafic activity in the SOA was believed to be comprised solely of dikes and sills, however rocks found in drilled wells showed that the mafic activity in the region was much more widespread. Mafic lavas were first described in the Hamilton Brothers #1-18 Turner Falls test well, drilled in 1981-1982 to a depth of 18,500 feet, and provided the first evidence of a much larger extent of mafic activity (Puckett et al., 2014). Evidence of mafic-intermediate lavas within the region have since been found in 21 drilled wells, and the proposed estimates of the magmatism produced has qualified the SOA as a large igneous province (LIP) and a potential flood basalt field (Hanson et al., 2012).

Based on the vast amount of erupted igneous material, one could imply a flood basalt event took place during the formation of the aulacogen. Flood basalts are defined by a large volume of volcanism produced over a relatively short period of time, and can form from purely upper-mantle processes (e.g., continental rifting) or processes that involve a component of lower mantle upwelling (e.g., a mantle plume) that forces continental rifting. Flood basalts tend to be composed of tholeiitic magmas, forming from the head of a mantle plume and categorized as

Ocean Island Basalts (OIB), regardless of whether they erupted in an oceanic or intracontinental setting (Hoffman, 1997).

OIB's can be defined further by their elemental composition. There are three types of OIB that are commonly recognized: HIMU, Enriched Mantle 1 (EMI), and Enriched Mantle 2 (EMII) (Weaver, 1991; Jackson and Dasgupta, 2008). OIB's are relatively enriched in incompatible trace elements (mobile elements in a melt) compared to Mid Ocean Ridge Basalt (MORB), which is composed of depleted upper-mantle melts (Hoffman, 1997). Weaver (1991) proposed that OIB's are primarily comprised of recycled oceanic crust that has undergone subduction and reintroduction into the mantle. The composition of the erupted basalt can vary depending on the mantle source. The difference between HIMU, EMI, and EMII magmas is determined by other contaminants in the melt. HIMU OIB shows little evidence of other types of contamination, while EMI and EMII OIBs show signatures of continental crust contaminants mixed in with the source melt. EMI OIB signatures show evidence of contamination by ancient pelagic sediment, and EMII OIB signatures represent recycled ancient terrigenous sediment (Weaver, 1991). Each of these mantle sources has a distinct isotopic signature. HIMU lavas have high Pb and Nd isotope ratios, and low Sr ratios. EMI lavas have low Pb and Nd ratios, and intermediate Sr ratios. EMII lavas have intermediate Pb ratios, low Nd ratios, and high Sr ratios (Jackson and Dasgupta, 2008).

Flood basalts are a subcategory of large igneous provinces (LIPs). Bond and Wignall (2014) classify LIPs as magmatic provinces with a volume greater than 100,000 km^3. Often attributed to the eruption of the head of a mantle plume, the largest flood basalt provinces (Siberian Traps, Ontong Java) have an average eruption period of between 25-40 Ma (Walker, 1993), while smaller flood basalt events, such as the Colombia River Basalt Group may occur in

under 5 Ma (Barry et al., 2010, Hooper, 2000). The entire formation of a flood basalt system may occur over multiple eruptions, represented by different lava packages. Chemostratigraphic analyses performed for this thesis and by Bulen (2012) show the potential for multiple lava packages within the SOA. Gamma ray logs used by Puckett (2011) show that, on average, mafic-intermediate lavas are 30-40 feet thick. The geology of the Arbuckle Mountains region of the SOA shows that these stratigraphically controlled lavas are found within thicker sections and are interbedded with rhyolite lavas, intrusive bodies, and rift-fill sedimentary strata (Hanson et al., 2012; Puckett et al., 2014).

Since each separate eruption in the flood basalt event produces such a large volume of magma, the output rate remains high even if the frequency is low (Walker, 1993). A lower eruption frequency would cause magmatic conduits to cool between different eruptive events, leading to the flood basalt packages that erupt along a variety of vents including fissures and shield volcanoes.

A common occurrence within rift zones and flood basalt fields is the emplacement of dike swarms (Walker, 1993). The SOA represents the failed arm of a triple junction rift system, and is composed of multiple layers of mafic-silicic lavas as well as multiple sets of intrusive mafic dikes (Puckett et al., 2014). Lidiak et al. (2014) explains that there are two suites of diabase dikes in the SOA. The first swarm is believed to have been emplaced slightly after the formation of the A-type basement granites during the Mesoproterozoic. The later dike swarm is believed to have intruded closer to the formation of the aulacogen. The younger dikes hold similar geochemical traits to basalts associated with LIPs (Lidiak et al., 2014). Lidiak et al. (2014) propose that the dikes "must have fed a volcanic field," however, over time the basaltic

field would have eroded away. Nonetheless, these diabase dikes act as local evidence towards the creation of voluminous mafic magmatism during the formation of the SOA.

Many locations throughout the SOA show geophysical anomalies greater than 100 mGal. These are attributed to large amounts of mafic volcanism in the subsurface (Keller and Stephenson, 2007) and this further supports the theory that the formation of the SOA was part of a flood basalt event.

Although geochronology is lacking to fully document the duration of magmatism, the amount of volcanism, evidence of flow packages, underlying dike swarms, and geophysical anomalies provide support for linking the SOA to a flood basalt event. Furthermore, this study, along with prior work by Bulen (2012) and Brueseke et al. (2014), provide new geochemical constraints on the SOA and this subsurface volcanic package, including the first Sr and Nd isotope data on extrusive mafic-intermediate lavas in the Arbuckle Mountains. While there is a lack of data defining the age of these melts, it is clear that the SOA represents a large igneous province. Whether it represents a flood basalt is still up for debate and requires more research, especially that focused on the timing of volcanism.

Geologic Background

There is a significant lack of exposed volcanic and plutonic rocks in the Arbuckle Mounains. The most recent of the major volcanic events in the region was the Cambrian Carlton Rhyolite, and while there are few exposures, they do occur throughout the SOA (Hanson et al., 2012, Hanson and Eschberger, 2014, Eschberger et al., 2014). The older Ancient felsic materials in the region consist of the Tishomingo and Troy Granites, Precambrian basement rocks over which the SOA formed (Hoffman et al., 1974, Denison et al., 1987). The only surficial evidence

of mafic material in the Arbuckle region is the two sets of dikes described by Lidiak et al. (2014).

The volcanic history of the Arbuckle Mountains is not well understood. The major mafic-intermediate lavas found during subsurface exploration are interbedded with rhyolite and sedimentary layers (Figure 1.2). These erupted basalts to andesites are believed to be early Cambrian in age (Hanson et al., 2012). Following the eruption of the Carlton Rhyolites, the SOA underwent erosion and a period of deposition of sediments. Throughout the remainder of the Paleozoic, the SOA was overturned and compressed, followed by faulting (Hoffman et al., 1974).

The mafic to intermediate lavas in the Arbuckle Mountains subsurface show some similarities to exposed gabbros in the Wichita Mountains. Known as the Roosevelt Gabbros, these plutons have compositions equivalent to hydrous, olivine tholeiites. The Roosevelt Gabbros intruded through the Glen Mountains Layered Complex around, a series of anhydrous, alumina-rich rocks that are interpreted to have crystallized from a tholeiitic parental magma, around 520-535 Ma (McConnell and Gilbert, 1990; Cameron et al., 1986). The formation of the Glen Mountains Layered Complex occurred as rifting in the SOA began. This layered complex extends for over 1,000 km^2, is 3-5 km thick, and is the oldest igneous event believed to be associated with the aulacogen (Hamilton et al., 2014).

Following an erosional period, there was a period of rhyolitic eruptions and the intrusion of granitic sills, known as the Wichita Granite Group (Keller and Stephenson, 2007). The silicic magmas that erupted as rhyolite lavas were likely formed from fractional crystallization of a large amount of basaltic magma underlying the SOA, as well as partial melting of the upper continental crust (Hanson and Al-Shaieb, 1980; Hanson et al., 2012; Hanson et al., 2014).

Thomas (2014) put forth a different hypothesis for the origin of the SOA by comparing the similar trends of the rift zone with the Alabama-Oklahoma transform fault. The intersection of both the SOA and the Alabama-Oklahoma transform fault with the Ouachita thrust fault may be reason to believe that the SOA formed as a leaky transform fault system (Thomas, 2006; 2014). The composition and geometry of SOA magmatism indicates crust-cutting, almost vertical fractures that have acted as conduits for magmatic eruptions. These fractures are expected within a leaky transform fault system, which, according to Thomas (2006, 2014), is similar to a bend in the Grenville front and also matches up with Precambrian mafic dikes found in the Arbuckle Mountains.

However, due to the volume of extrusive lavas inferred to exist in the subsurface, the hypothesis that the SOA represents a mafic LIP or volcanism related to rifting makes the most sense. As with all lavas, the geochemistry will give significant insight into defining potential mantle sources involved in magmatism, and deciphering these sources is a key to understanding more about the mafic to intermediate lavas in the SOA. As with most mafic LIPs, one could expect the prevalence of an OIB-type mantle source. Utilizing bulk major and trace element analyses determined by x-ray fluorescence (XRF), Sr and Nd isotope analyses via thermal ionization mass spectrometry (TIMS), and rare earth element analyses via inductively coupled plasma mass spectrometry (ICP-MS), this study provides new insights into the petrologic constraints on the volcanic event that helped shape the region as well as potential mantle sources involved in SOA mafic magmatism.

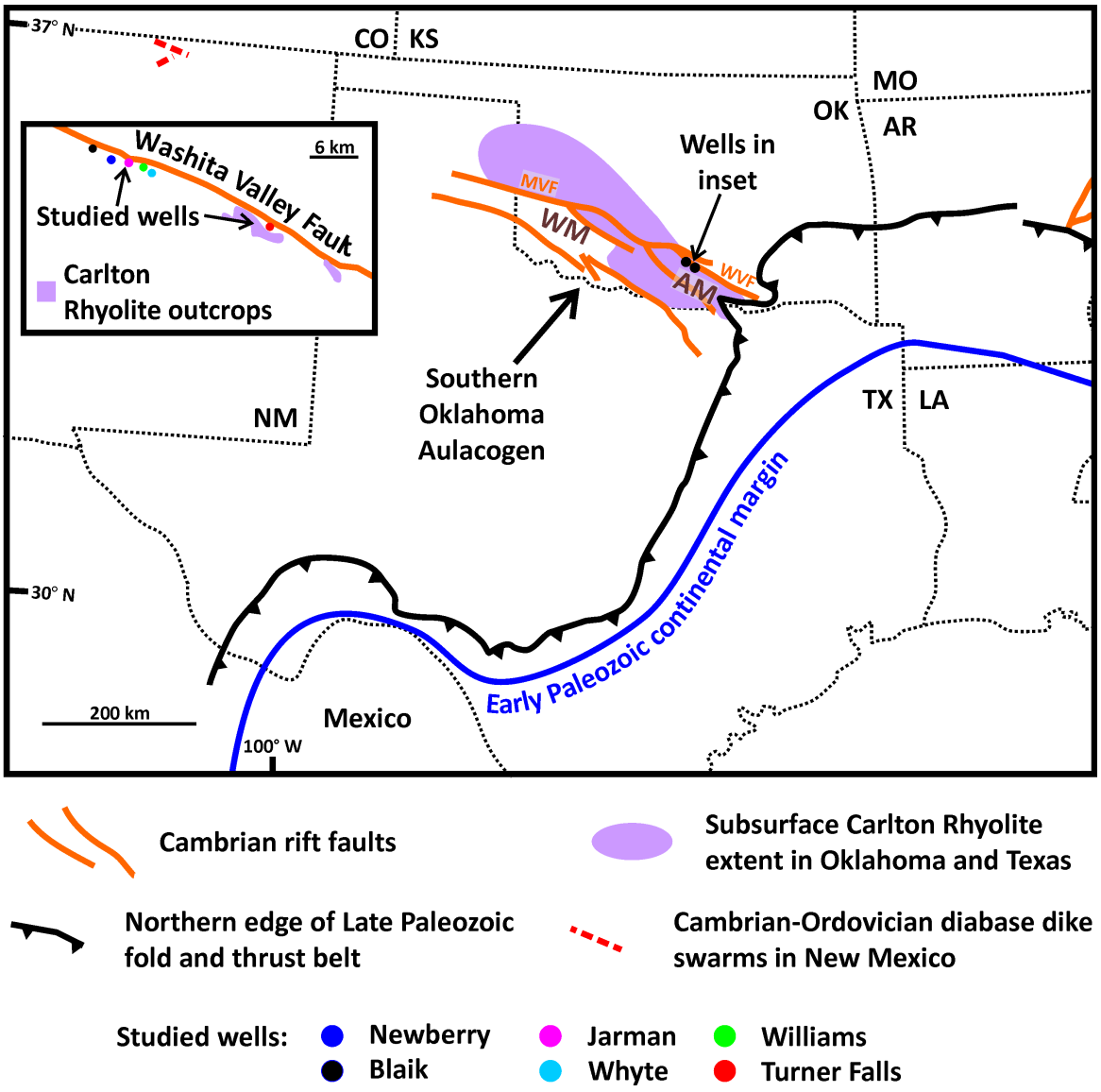

Figure 1.1 Map of the Southern Oklahoma aulacogen (Hanson et al. 2012).
The extent of the Southern Oklahoma aulacogen through the Arbuckle and Wichita Mountains, including potentially related dike swarms located in northern New Mexico. The inset shows the Washita Valley Fault, along with the locations of wells drilled during oil and gas exploration that have been sampled.

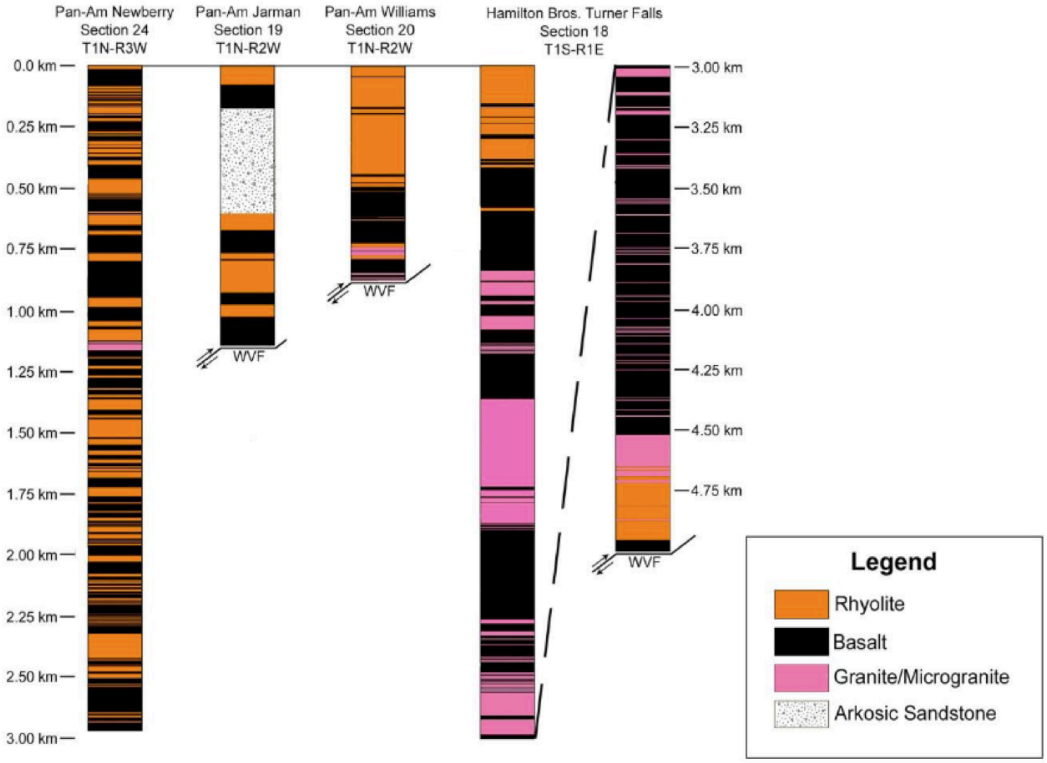

Figure 1.2 Lithologic well logs of the igneous and sedimentary stratigraphy of wells studied in this thesis and Bulen (2012), adapted from Puckett et al. (2014).

Chapter 2 - Methods

Samples of well cuttings were collected from four wells in the Western Arbuckle Mountains region: Pan-Am Whyte Unit #1 (SE NE SW, sec. 21, T. 1N., R. 2W), Blaik Oil Co. #1 B-13 Mauldin (NW NW, sec. 15, T. 1N., R. 3W.), Union Oil Co. of California #1-31 Morton (NE SW NE, sec. 31, T. 1N., R. 1W.), and the Hamilton Brothers Oil Co. #1A-18 Turner Falls (SE NE NW SW, sec. 18, T. 1S., R. 1E.). Samples were collected from the Oklahoma Geological Survey sample library at the Oklahoma Petroleum Information Center in Norman, Oklahoma. These wells were chosen for the thickness of the mafic packages, and the depths from which the samples were picked were chosen based on the amount of sample, size of the cuttings, and the amount of mafic material visible under binocular microscope. 56 samples were collected in total (15 samples from the Turner Falls, 10 from the Morton, 10 from the Blaik, and 21 from the Whyte). Due to the small grain size and contamination from other layers within the cuttings, samples from the Morton well were not analyzed.

Samples were prepared at Kansas State University for major and trace element analysis by x-ray fluorescence (XRF), thermal ionization mass spectrometry (TIMS) for Sr and Nd isotope analyses, and inductively coupled plasma mass spectrometry (ICP-MS) for rare earth element analyses. The samples were handpicked using a research grade binocular microscope to remove any foreign rocks and/or altered rock cuttings, with the goal of ensuring that only petrographically homogeneous mafic rock fragments remained for further crushing. This step removed any felsic material present in cuttings, as well as any obviously altered grains or mineral fragments. After handpicking, samples containing more than 8 g of

rock cuttings were crushed to a clay size (<200 mesh-sieve size) fraction in a Spex Industries aluminum oxide shatterbox.

Samples were sent to Franklin and Marshall College for XRF analysis to obtain major and trace element compositions and loss on ignition (LOI) values. Samples were analyzed following the method outlined in Mertzman (2000) and online at http://www.fandm.edu/earth-and-environment/x-ray-laboratory.

One-gram of rock powder from each sample was weighed to four decimals and placed in clean ceramic crucibles. The crucibles were heated at 900° C in a muffle furnace for 60-75 minutes. The samples cooled to room temperature and were reweighed. The change in percentage of sample was reported as loss on ignition (LOI). Following LOI analyses, 0.4000 grams of powder was mixed with 3.6000 grams of lithium tetraborate ($Li_2B_4O_7$) and melted in 95% Pt -5% Au crucibles. Once quenched into homogeneous glass disks, these melts were used for XRF analysis of major elements. Major elements were analyzed using a Panalytical, Inc. 2404 XRF vacuum spectrometer equipped with a 4 kW Rh x- ray tube. Major elements (SiO_2, Al_2O_3, CaO, K_2O, P_2O_5, TiO_2, Fe_2O_3, MnO, Na_2O, and MgO) are presented as weight percent oxide. Nineteen trace elements (Rb, Sr, Y, Zr, Nb, Ni, Ga, Cu, Zn, U, Th, Co, Pb, Sc, Cr, V, La, Ce, and Ba) were analyzed using the same XRF instrumentation used in the major element analysis process. A mixture of 7.000 g of whole-rock sample powder and 1.4000 grams of high purity Copolywax powder was used to create pressed powder briquettes for XRF analysis of trace elements. The Copolywax powder acts as a binding agent allowing for the formation of the briquettes. Trace element concentrations are presented as parts per million (ppm). Samples were then normalized to account for FeO and Fe_2O_3 from a total Fe_2O_3 (LeMaitre, 1976).

Whole rock Sr and Nd isotope analyses were performed using thermal ionization mass spectrometry (TIMS) at the University of Kansas on a subset of seven samples previously studied by Bulen (2012). These samples are CB-PAJ-10, CB-PAJ-13, CB-PAN-8, CB-PAN-16, CB-PAN-20, CB-PAW-1, and CB-PAW-14 and represent samples from three wells in the SOA: Pan-Am Jarman #1-19 (C NE NW NE, sec. 19, T. 1N., R. 2W.), Pan-Am Newberry Unit #1 (E2 NW NE NW, sec. 24, T. 1N., R. 3W.), and Pan-Am Williams D-2 (NE SE NW, sec. 20, T. 1N., R. 2W.) (Figure 2.1). Samples were prepped for analysis by using standard HF-HNO_3 and HCl dissolution techniques. Elemental separation was done using ion exchange columns. Sr was isolated and collected using cation exchange columns with Biorad resin. Nd and Sm were purified using Eichrome LN spec resin columns.

Samples were analyzed following the procedures of Krogh (1982), and Patchett and Ruiz (1987), details may be found at https://geo.ku.edu/tims-details. Analyses for Sr and Nd were completed on VG Sector 54, with internal and external precisions of ± 20 ppm. After correcting for fractionation using $^{86}Sr/^{88}Sr$=0.1194, Sr ratios are referenced to a value of 0.710250 for the $^{87}Sr/^{86}Sr$ ratio of NBS987. Measured laboratory value was 0.710247 on NBS987 over a 53 run period of analysis. Nd ratios were corrected by using a value of 0.511860 for $^{143}Nd/^{144}Nd$, following the standard set by LaJolla. A $^{146}Nd/^{144}Nd$ ratio of 0.7219 was used to correct for fractionation.

Rare earth element (REE) analyses were performed at Miami University (Ohio) by inductively coupled plasma mass spectrometry (ICP-MS). 10 samples were selected for REE analyses: the seven that underwent isotope analyses, as well as JH-14-12, JH-14-16, and JH-14-40. 75 mg of a 3:2 mixture of sodium tetraborate and potassium carbonate was used as a flux and mixed with 50 mg of powder from each sample. This mixture was heated at 950°C for 30

minutes in a graphite crucible. After cooling, the mixture was moved to an acid-washed, low density, polyethylene bottle, containing 125 ml of 1% HNO_3. The samples were allowed to dissolve overnight. Following dissolution, samples were then analyzed using a Varian "Red Top" ICP-MS. The ICP-MS was calibrated and internal standardization utilized a 100 ppb solution of Ge, Re, Bi, and In. For each sample, three runs of 30 readings were completed.

Alteration

As previously mentioned, some of the samples showed signs of alteration. Puckett (2011) reported that the samples found in the Turner Falls well were partially altered through multiple processes, including carbonate replacement of plagioclase, chloritization of matrix minerals, and epidotization of mafic minerals. Although cuttings that showed alteration were removed during the cleaning and preparation phase, it is possible that the results were still affected by alteration.

To rule out potential alteration affects on the geochemistry of these samples, an "alteration filter" was applied. Beswick and Soucie (1978) proposed an "alteration filter" that seeks to determine the amount of alteration that an igneous sample has undergone. Significant alteration of a sample would affect the interpretation of geochemical data. This "alteration filter" plots molecular proportions of major element ratios (Al_2O_3/K_2O, SiO_2/K_2O, CaO/K_2O, etc.) on a logarithmic XY-plot (Beswick and Soucie, 1978). Samples plotted on a logarithmic scale, will appear clustered in linear array if they are unaltered. Any significant variation from this linear array is suggestive of post-eruptive alteration in the samples and these samples will not be discussed as part of this project. Two samples (JH-14-21, JH-14-22) did not fall along the linear array on multiple plots that used the alteration filter (Figure C.1**)**. These samples have been classified as "significantly altered." Both of these samples have been removed from the final

interpretations and any discussion/diagrams in this thesis. Samples from the Turner Falls well all yielded identical geochemical results; thus they have been averaged into one representative sample: TF-AVG that is representative of the geochemistry in the sampled portion of this well. A full list of the Turner Falls samples can be found in Appendix D.

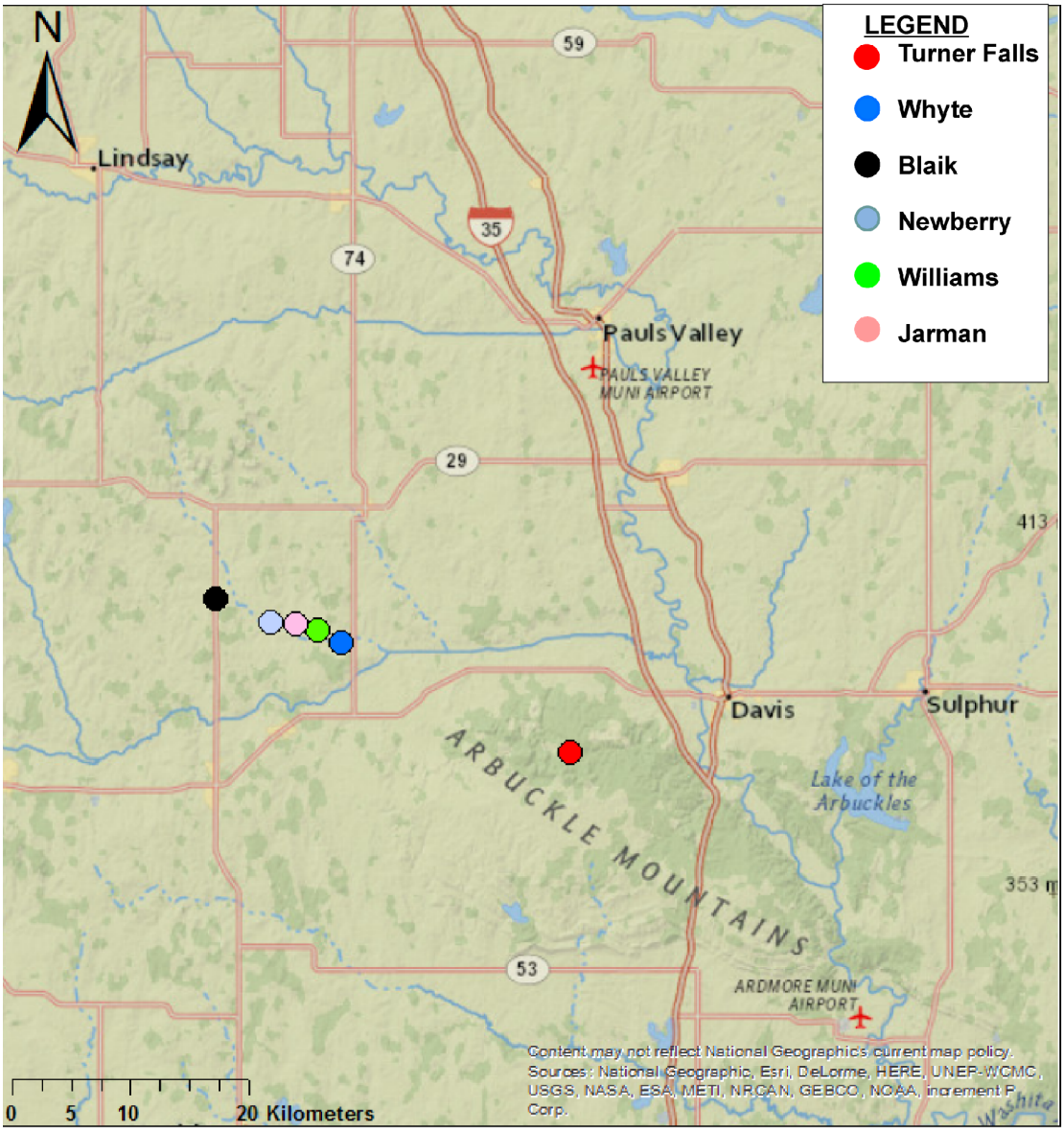

Figure 2.1 Sampled Wells in the Arbuckle Mountains

The locations of the three wells sampled in this study (Turner Falls, Whyte, Blaik), and the three wells originally studied by Bulen (2012) (Newberry, Williams, Jarman).

Chapter 3 - Results

Major and trace element geochemical data were obtained on 29 samples of subsurface mafic rocks from three wells present in the Southern Oklahoma aulacogen. Major element data are reported in weight percent (wt. %) oxide and trace element data in parts per million (ppm). A complete list of samples can be found in Appendix A; major and trace element data are reported in Appendix B. Representative data from these three wells are presented in Table 3.1. Sr and Nd isotope analyses were collected on seven samples (Table 3.2) and rare earth element analyses for ten samples from the Arbuckle Mountains (Table 3.3.

Geochemical Classification

On the total alkalis versus silica (TAS) diagram of Le Bas et al. (1986), samples plot as subalkaline to transitional (trachy-)basalts to (trachy-)andesites, with SiO_2 values ranging from 48.95 to 57.88 wt. % (Figure 3.1). The samples lie along a positive linear trend with increasing alkali contents as silica content increases and are subalkaline to transitional.

The Zr/TiO_2 versus Nb/Y diagram used by Winchester and Floyd (1977) to classify igneous rocks is shown in Figure 3.2. The well cuttings plot as subalkaline-alkaline basalts, as well as on the boundary of more transitional rocks. This reinforces the interpretation of the Le Bas et al. (1986) total alkalis vs silica plot, and also indicates that the any alteration the samples have undergone has had little effect on the bulk chemistry. This diagram utilizes four high-field-strength elements (HFSE), which tend to be resistant to the affect of low-T alteratio (e.g., they are fluid immobile). This provides substantial support to the results of the TAS diagram.

The samples plot as tholeiitic on the FeO*/MgO versus silica discrimination diagram used by Miyashiro (1974; Figure 3.3). This interpretation is mostly supported on the AFM diagram (Irvine and Baragar, 1971) with the majority of samples plotting in the tholeiitic field (Figure 3.4). However, some samples with higher wt. % MgO plot just under the calc-alkaline field, but along a similar trend associated with tholeiitic magmas. Discrimination diagrams that utilize immobile trace elements consistently depict the samples as mostly tholeiitic to transitional, supporting the major element data. On the discrimination diagram of Pearce (1982), which plots Nb/Y vs Ti/Y, the samples plot as tholeiitic to transitional (Figure 3.5). Figure 3.6 shows the well cuttings on the Nb/Y versus $Zr/P_2O_5 \times 10^4$ diagram presented by Floyd and Winchester (1975). This diagram indicates that the samples are tholeiitic, with the exception of the Turner Falls sample, which plots as alkali basalt. Some samples, such as the Turner Falls sample in figure 3.6, plot as an alkali basalt in one diagram, but as tholeiitic or transitional in others. Due to this variation, it is believed that these alkali samples are in reality more transitional in nature.

Major and Trace Element Geochemical Characteristics

Harker diagrams for the major elements (wt. %) plotted versus SiO_2 (wt. %) can be seen in Figure 3.7. There is no linear array for Al_2O_3. Al_2O_3 concentrations range from 12.70 to 15.06 wt. %.Negative linear arrays exist in plots that compare Al_2O_3, FeO*, MgO, TiO_2, and CaO with SiO_2. FeO concentrations range from 6.38 to 8.85 wt.%, and Fe_2O_3 concentrations range from 4.97 to 6.02 wt. %. CaO values range from 4.74 to 9.11 wt. %, and MgO values range from 3.24 to 7.07 wt. %. TiO_2 concentrations range from 1.65 to 3.29 wt. %, and while negative linear arrays are obvious on this diagram, the samples from the Blaik Mauldin well and those from the Pan-Am Whyte and Turner Falls wells plot

separately from one another. TiO_2 concentrations of the Blaik well range from 2.60 to 3.29 wt. %, while samples from the Whyte and Turner Falls well have TiO_2 concentrations that range from 1.65 to 2.26 wt. %. Total alkali (Na_2O and K_2O) concentrations show an increase with SiO_2. Na_2O concentrations range from 2.90 to 4.47 wt. %, and K_2O concentrations range from 0.73 to 2.44 wt. %. P_2O_5 shows a constant relationship with silica, with concentrations ranging from 0.26 to 0.46 wt. %. However there is a noticeable difference in the P_2O_5 concentrations of each well, with the Blaik well having concentrations above ~0.40 wt. %, and the Whyte well having concentrations below 0.34 wt. %. The Turner Falls sample has a P_2O_5 concentration of 0.40 wt. %.

There are a few samples from the Whyte well between 50 and 52 wt. %. SiO_2 that have uncharacteristically low CaO and high Al_2O_3. This may be due to fractionation during the cooling process or alteration during the drilling of the wells.

Samples from the Whyte well range to the highest concentrations of SiO_2 observed in the suite (54-56 wt. %), while the Turner Falls sample contains the lowest concentration. However, the ranges for Blaik and Whyte wells overlap and there is no statistical distinction in silica content between the wells.

Trace element concentrations (in ppm) are plotted against wt. % SiO_2 in Figures 3.8 and 3.9. For Cr and Cu the Turner Falls sample represents an outlier. Some of these elements exhibit subparallel arrays between samples from different wells.

Non-linear relationships occur between silica and rubidium, barium, and niobium. These relationships have minimal correlation, but are in general, broadly positive. There is positive correlation visible between Nb and SiO_2 for Blaik samples. Concentrations range from

11.40 to 55.80 ppm for Rb, 307 to 554 ppm for Ba with an outlier of 181 ppm, and 20.20 to 39.30 ppm for Nb.

Cerium, lanthanum, zirconium, and yttrium concentrations depict broadly positive linear relationships with silica, although the samples from Whyte and Blaik for separate arrays in some cases (e.g., Zr, Ce). Concentrations range from 25 to 60 ppm for Ce, 12 to 27 ppm for La, 140 to 400 ppm for Zr, and 27.25 to 49.50 ppm for Y. Subparallel arrays are visible on the Zr, La, and Ce versus silica diagrams. Zr, La, and Y have clusters from Whyte samples at varying depths, while Ce has visible clusters in both the Whyte and Blaik wells. Examples of this can be seen in figure 4.13 and 4.14. Broadly negative relationships exist between silica and strontium, copper, and vanadium. Concentrations range from 99.42 to 184 ppm for Cu, 240 to 373 ppm for V, and Sr concentrations range from 203 to 432 ppm.

Nickel, cobalt, scandium, and chromium display relatively well defined negative correlations with silica. Contents vary from 39 to 63 ppm for Co, 36 to 169 ppm for Cr, with an outlier of 304, and Sc values of 24 to 39 ppm with an outlier of 9. Concentrations are more scattered for chromium, especially at lower silica concentrations. Samples from these wells have Ni concentrations ranging from 31 to 98 ppm. Samples from subsequent depths in the Blaik and Whyte well form separate clusters on the Ni versus SiO_2 diagram, with the Whyte clusters being easier to discern (Figure 4.13, 4.14). Scandium concentrations show similar relationships as they decrease with increasing silica and the Whyte well has clusters with samples from subsequent depths. In general, these clusters occur with the same samples with similar nickel and scandium concentrations.

Zinc and lead concentrations in each sample are fairly low. Zn concentrations range from

124 to 181 ppm and Pb concentrations range from <1 to 13 ppm. Both Zn and Pb are relatively scattered when plotted versus silica and have clear clusters formed when plotted with depth for both the Blaik and the Whyte wells.

Isotopic Analysis

Isotopic analysis was completed for Sr and Nd isotope ratios on a subset of samples previously studied in Bulen (2012). Analysis was completed by TIMS at the University of Kansas. Seven samples from three wells (Pan-Am Jarman, Pan-Am, Williams, and Pan-Am Newberry) with varying wt. % SiO_2 were chosen to give a well-rounded understanding of the study area (Figure 3.10). Two samples were taken from Pan-Am Williams (CB-PAW-1, CB-PAW-14) with a lower silica content (51.94 to 53.55), two samples were taken from Pan-Am Jarman (CB-PAJ-10, CB-PAJ-13) with a high silica content (56.34 to 61.16), and 3 samples were taken from Pan-Am Newberry (CB-PAN-8, CB-PAN-16, CB-PAN-20), which cover the entire spread. One sample, CB-PAN-8, does not have a $^{144}Nd/^{143}Nd$ value due to errors with the TIMS analysis.

$^{87}Sr/^{86}Sr_i$ and $^{144}Nd/^{143}Nd$ values have been age corrected to 535 Ma. Overall, $^{87}Sr/^{86}Sr_i$ values range from 0.703970 to 0.706403, and $^{144}Nd/^{143}Nd$ values range from 0.512051 to 0.512162. Epsilon Nd values range from 1.67 to 3.86. The Williams well contains samples that have moderate $^{87}Sr/86Sr_i$ values and low $^{144}Nd/^{143}Nd$ values. CB-PAW-1 has an $^{87}Sr/^{86}Sr_i$ value of 0.705296, a $^{144}Nd/^{143}Nd$ value of 0.512131, and an epsilon Nd value of 3.22. CB-PAW-14 has an $^{87}Sr/^{86}Sr_i$ value of 0.705229, a $^{144}Nd/^{143}Nd$ value of 0.512051, and an epsilon Nd value of 1.67.

The Jarman well contains the highest $^{87}Sr/^{86}Sr_i$ values and moderate $^{144}Nd/^{143}Nd$ values. CB-PAJ-10 has an $^{87}Sr/^{86}Sr_i$ value of 0.706403, a $^{144}Nd/^{143}Nd$ value of 0.512101, and an epsilon

Nd value of 2.60. CB-PAJ-13 has an $^{87}Sr/^{86}Sr_i$ value of 0.704971, a $^{144}Nd/^{143}Nd$ value of 0.512129, and an epsilon Nd value of 3.16.

Samples from the Newberry well have the lowest $^{87}Sr/^{86}Sr_i$ values and the highest $^{144}Nd/^{143}Nd$ sample, as well as one sample with no Nd data. CB-PAN-8 has an $^{87}Sr/^{86}Sr_i$ value of 0.704660 and no $^{144}Nd/^{143}Nd$ value. CB-PAN-16 has an $^{87}Sr/^{86}Sr_i$ value of 0.705014, a $^{144}Nd/^{143}Nd$ value of 0.512063, and an epsilon Nd value of 1.87. CB-PAN-20 has an $^{87}Sr/^{86}Sr_i$ value of 0.703970, a $^{144}Nd/^{143}Nd$ value of 0.512162, and an epsilon Nd value of 3.86.

Rare Earth Element Analysis

Rare Earth Element analysis was completed by inductively coupled plasma mass spectrometry (ICP-MS). Ten samples were selected by varying wt. % SiO_2 to give a broad example of the study area. The seven samples that underwent isotope analyses, JH-14-12, JH-14-16, and JH-14-40 were chosen. The Arbuckle samples are enriched in light rare earth elements (LREE) compared to the heavy rare earth elements (HREE). The LREE are La, Ce, Pr, Nd, Sm, Eu, and Gd. La values range from 14.98 to 49.55 ppm, Ce values range from 34.75 to 113.13 ppm, Pr values range from 5.51 to 14.49 ppm, and Nd values range from 25.37 to 61.68 ppm. Sm, Eu, and Gd values are lower than the other LREE, but higher than the HREE. Sm values range from 5.92 to 15.66 ppm, Eu values range from 1.62 to 3.77 ppm, and Gd values range from 6.15 to 15.50 ppm.

HREE are Tb, Dy, Ho, Er, Tm, Yb, and Lu. Tb values range from 0.98 to 2.43 ppm, Dy values range from 5.64 to 13.69 ppm, Ho values range from 1.10 to 2.67 ppm, Er values range from 3.04 to 7.45 ppm, Tm values range from 0.42 to 1.02 ppm, Yb values range from 2.63 to 6.48 ppm, and Lu values range from 0.39 to 0.94 ppm.

CB-PAN-16 had the highest values for all of the REEs, and CB-PAN-20 had the lowest values for all of the REEs besides Eu. The Arbuckle Samples show negative Pr and Eu anomalies, and is enriched in Er and Yb compared to the other HREE.

Table 3.1 Major element and trace element raw data for well cutting samples from the Arbuckle Mountains.

Major element data is given in weight percent oxide and trace element data is given in parts per million. For analysis of all samples, see appendices.

	JH14-12	JH14-16	JH14-26	JH14-29	JH14-40	TF-AVG
SiO_2	57.88	50.53	51.68	50.97	55.74	48.95
TiO_2	2.60	3.14	2.21	2.17	1.65	2.12
Al_2O_3	12.78	13.34	14.24	14.60	13.28	14.59
Fe_2O_3	4.97	5.60	5.16	5.08	5.20	12.42
FeO	6.38	8.53	7.68	7.64	6.89	
MnO	0.19	0.29	0.21	0.21	0.20	0.19
MgO	3.24	5.39	6.80	6.84	3.57	6.49
CaO	5.10	6.52	5.56	6.02	6.62	9.08
Na_2O	3.44	3.76	3.94	3.87	4.23	3.20
K_2O	2.34	1.49	1.36	1.44	1.52	1.04
P_2O_5	0.37	0.46	0.29	0.31	0.33	0.40
Total	100.00	100.00	100.00	100.00	100.00	
LOI	2.55	2.84	5.42	5.86	1.15	
Ba	501	481	416	411	464	510
Ce	41	29	37	31	52	50
Co	39	56	61	58	46	
Cr	53	85	80	133	45	304
Cu	117	158	174	153	159	99
Ga	20.4	18.1	17.1	17.1	18.6	
La	25	15	12	13	27	21
Nb	39.3	27.3	27.5	26.8	31.4	24
Ni	31	59	67	68	36	97
Pb	10	<1	13	<1	<1	
Rb	48.1	29.5	17.4	21.5	25.2	23.6
Sc	24	30	35	36	30	33
Sr	290	328	203	263	232	527
Th	4.8	1.1	8.1	10.0	6.2	
U	0.8	0.9	<0.5	<0.5	<0.5	
V	240	305	299	344	282	265
Y	49.5	38.0	35.2	34.5	49.2	27.3
Zn	156	139	181	158	131	
Zr	400	217	175	179	299	140

Table 3.2 Sr and Nd isotope data for the seven samples analyzed in this study, along with SiO_2 in weight percent.

Sample	SiO_2	$^{87}Sr/^{86}Sr_i$	$^{143}Nd/^{144}Nd_i$
CB-PAW-1	51.94	0.705296	0.512157
CB-PAW-14	53.55	0.705229	0.512077
CB-PAN-8	55.23	0.704660	
CB-PAN-16	61.32	0.705014	0.512088
CB-PAN-20	47.58	0.703970	0.512190
CB-PAJ-10	61.16	0.706403	0.512125
CB-PAJ-13	56.34	0.704971	0.512154

Table 3.3 Rare Earth Element data for the ten samples analyzed in this study.

Sample	JH14-12	JH14-16	JH14-40	CB-PAW-1	CB-PAW-19
La	40.12	25.23	31.30	19.41	30.33
Ce	91.15	59.31	69.58	44.63	70.07
Pr	11.22	8.44	8.85	6.67	9.10
Nd	49.37	40.42	39.83	29.59	44.70
Sm	11.28	9.36	6.92	6.62	10.23
Eu	2.62	2.78	1.76	2.18	2.79
Gd	11.67	9.30	7.93	6.55	10.40
Tb	1.92	1.45	1.46	1.02	1.66
Dy	11.14	8.25	9.03	5.90	9.76
Ho	2.20	1.60	1.85	1.17	1.97
Er	6.23	4.45	5.36	3.32	5.67
Tm	0.87	0.61	0.78	0.46	0.80
Yb	5.55	3.85	4.95	3.00	5.14
Lu	0.81	0.56	0.74	0.45	0.77
Sample	CB-PAN-8	CB-PAN-16	CB-PAN-20	CB-PAJ-10	CB-PAJ-13
La	33.10	51.24	15.62	33.82	26.02
Ce	76.09	116.88	36.19	76.98	58.65
Pr	9.50	14.49	5.51	9.04	7.93
Nd	46.19	61.68	25.36	40.38	34.13
Sm	9.57	15.66	5.92	6.90	6.25
Eu	2.51	3.77	2.24	1.62	1.69
Gd	10.05	15.49	6.15	7.75	7.03
Tb	1.65	2.43	0.98	1.41	1.23
Dy	9.53	13.69	5.63	8.77	7.51
Ho	1.87	2.67	1.10	1.81	1.54
Er	5.25	7.45	3.036	5.29	4.48
Tm	0.72	1.02	0.41	0.76	0.64
Yb	4.60	6.48	2.63	4.91	4.17
Lu	0.67	0.94	0.39	0.73	0.62

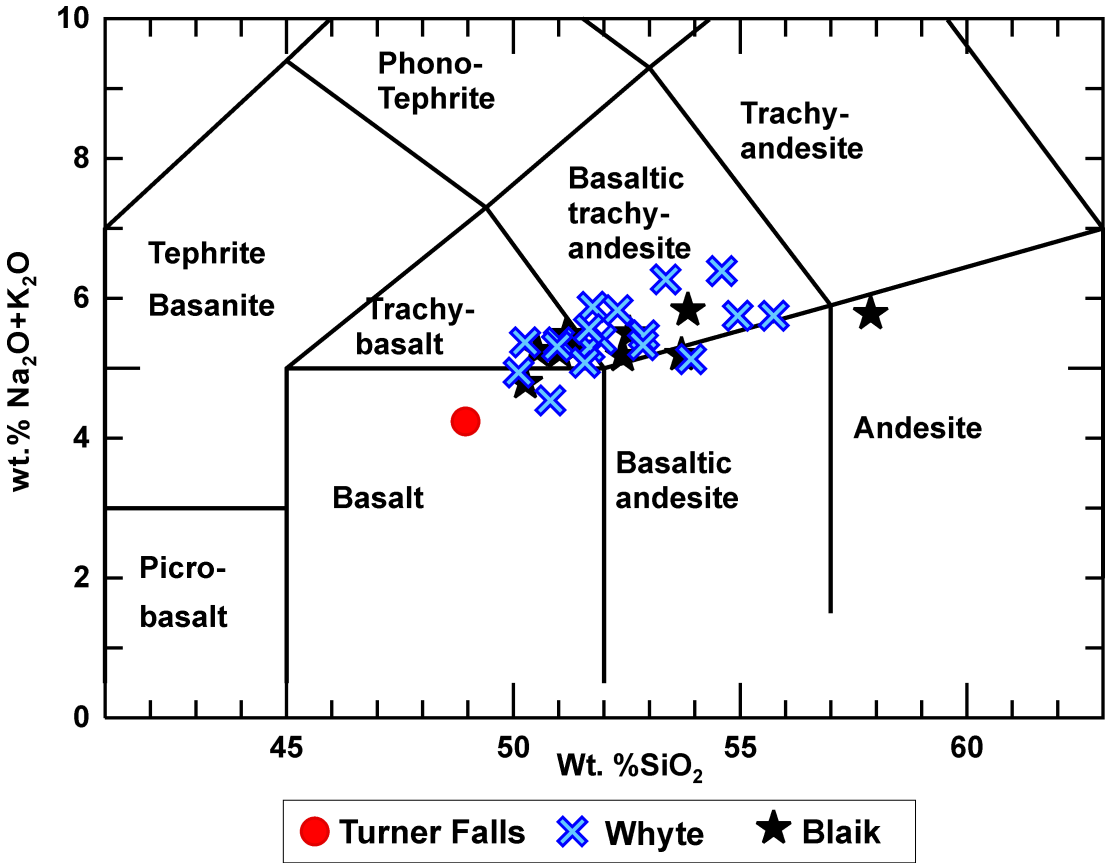

Figure 3.1 Total alkalis vs. silica diagram of LeBas et al. (1986).
Rock classification diagram using major element concentrations. Samples plot as Basalts to Andesites and Trachy-basalts to Trachy-andesites.

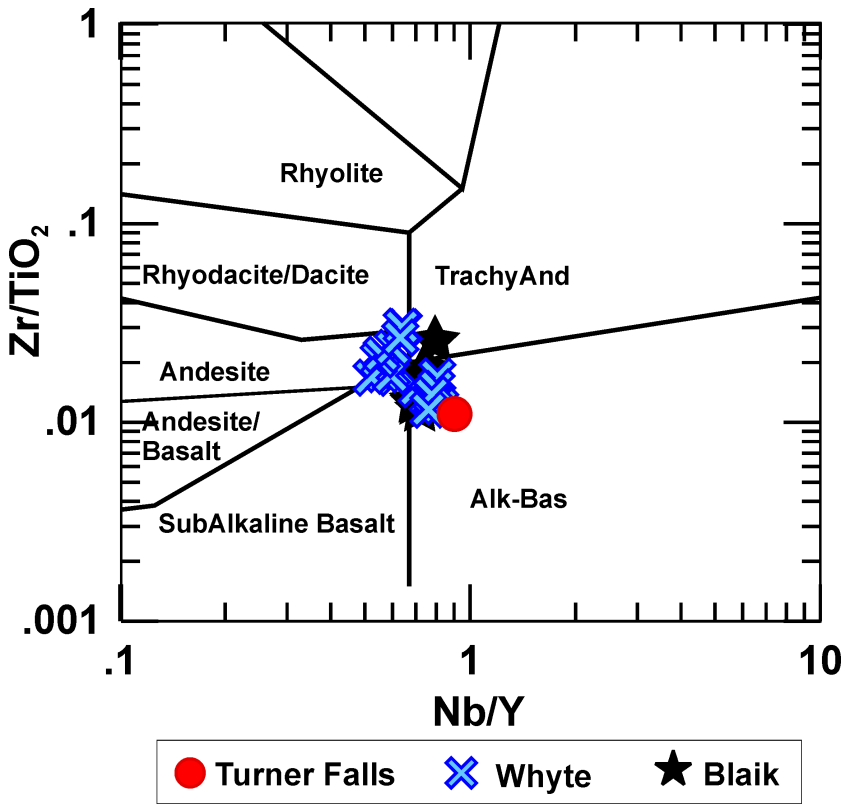

Figure 3.2 Nb/Y vs. Zr/TIO_2 discrimination diagram of Winchester and Floyd (1977)

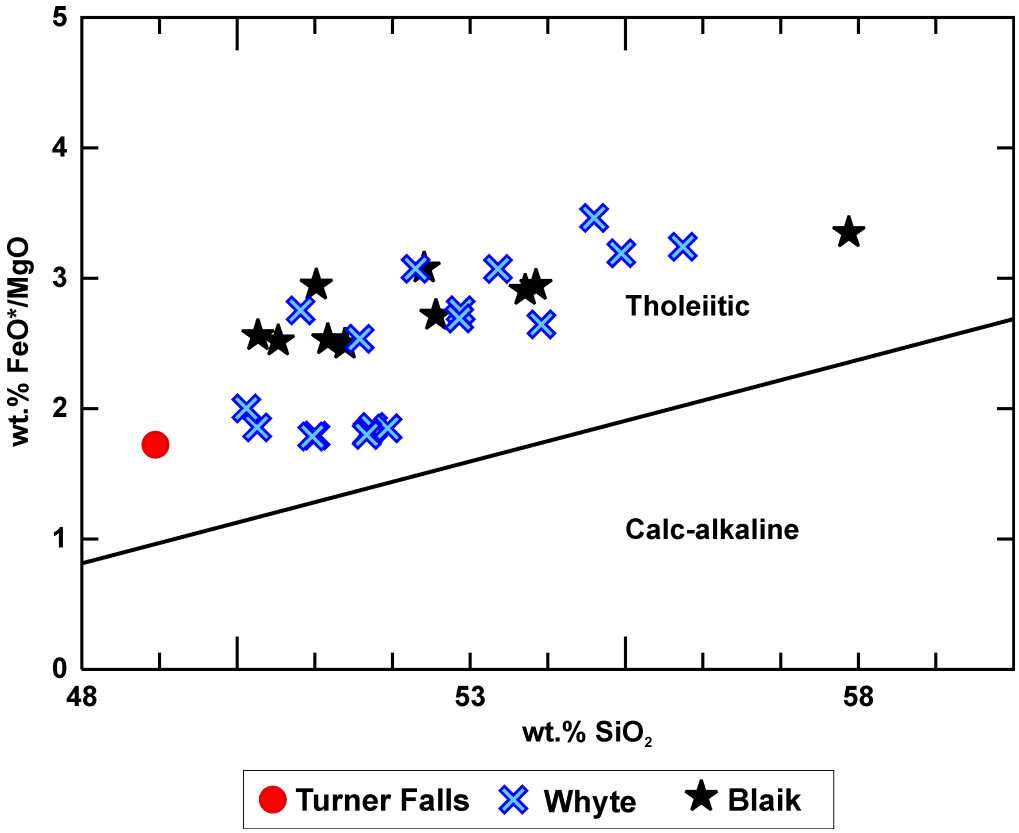

Figure 3.3 Discrimination diagram of Miyashiro (1974) used to distinguish between tholeiitic and calc-alkaline magmas.

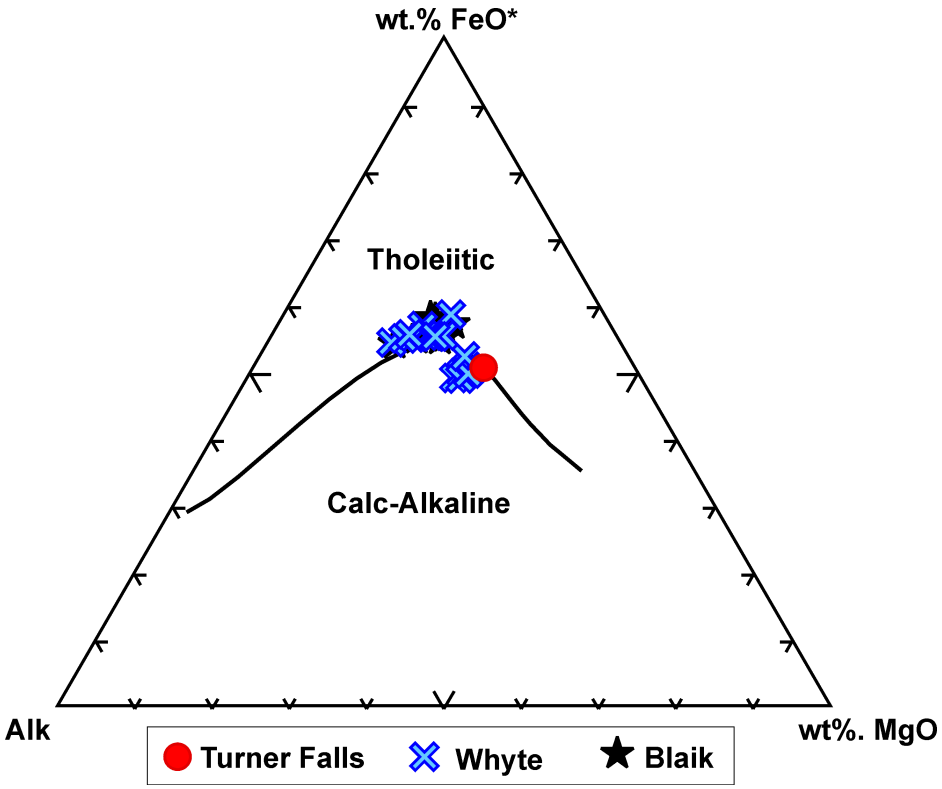

Figure 3.4 AFM diagram of Irvine and Baragar (1971)

This diagram distinguishes samples between tholeiitic and calc-alkaline by utilizing total alkalis, iron concentration, and magnesium concentration.

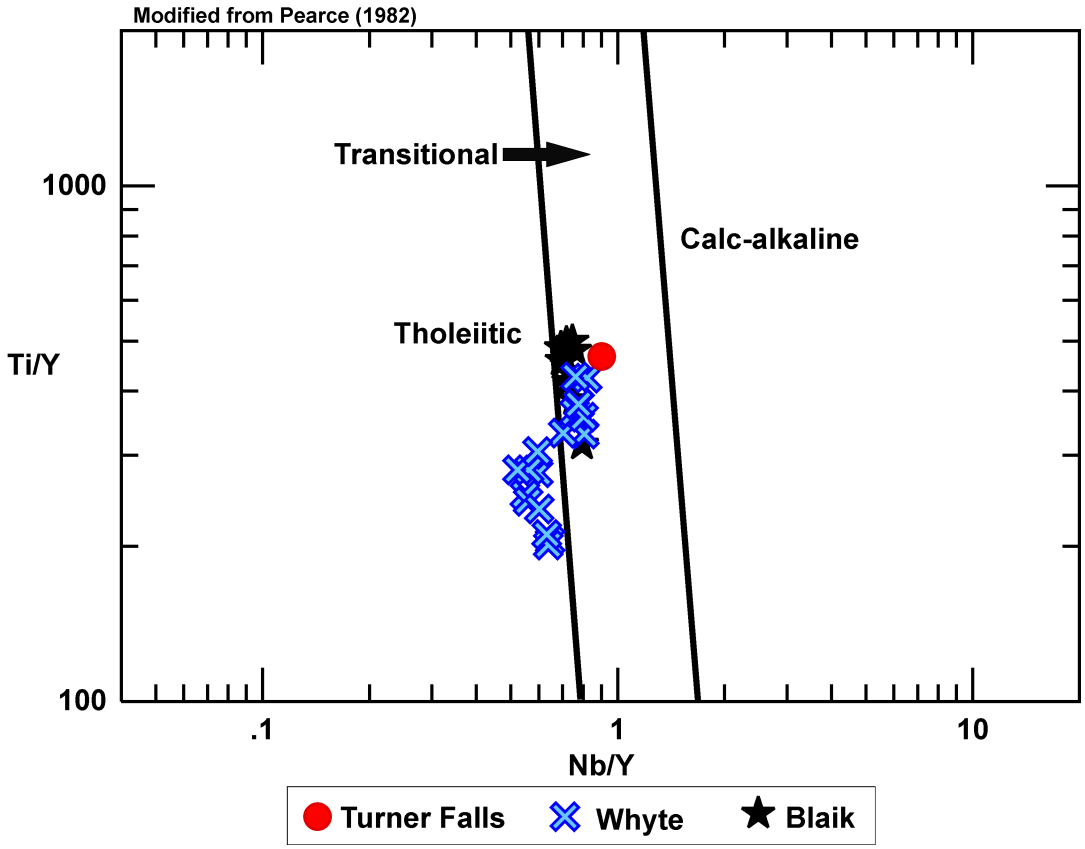

Figure 3.5 Discrimination diagram modified from Pearce (1982).
Used to distinguish between tholeiitic and calc-alkaline magmas, this figure shows that magmas plot as tholeiitic to tholeiitic-transitional.

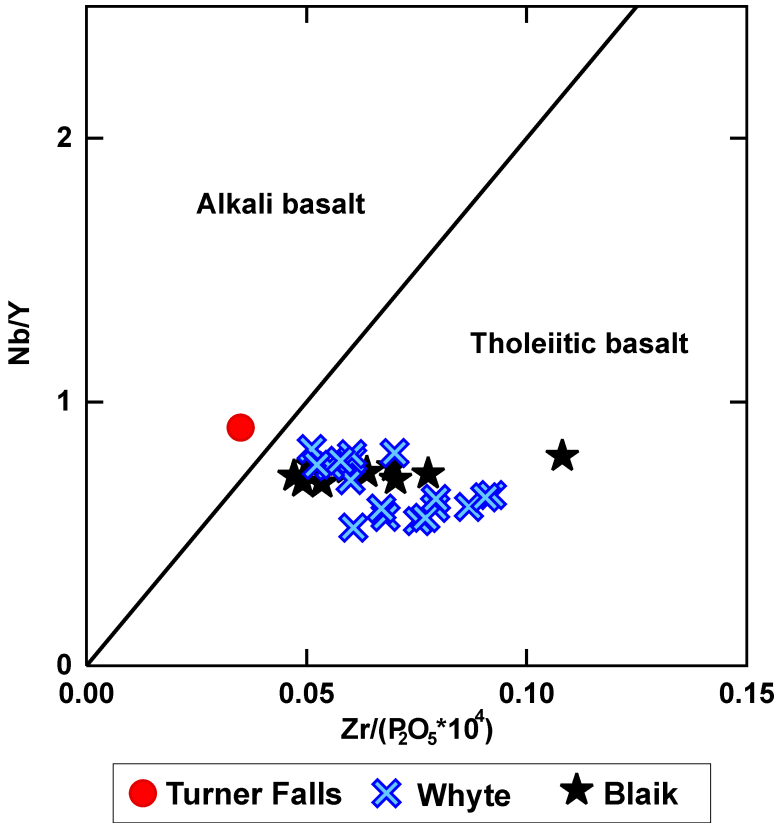

Figure 3.6 Discrimination diagram modified from Floyd and Winchester (1975).
Uses incompatible trace elements to distinguish between tholeiitic and alkali basalts.

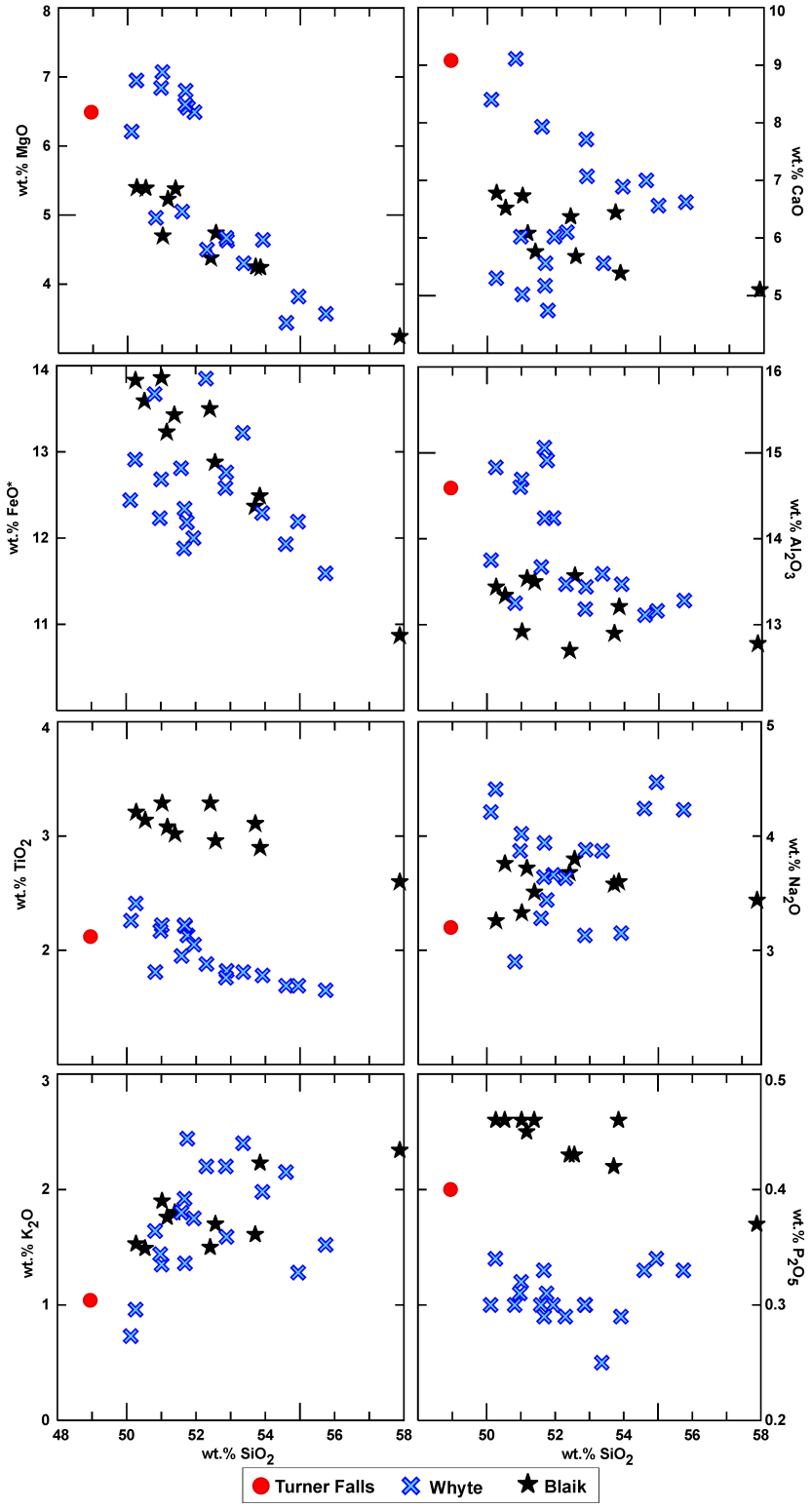

Figure 3.7 Harker diagrams showing major element concentrations in wt.%.

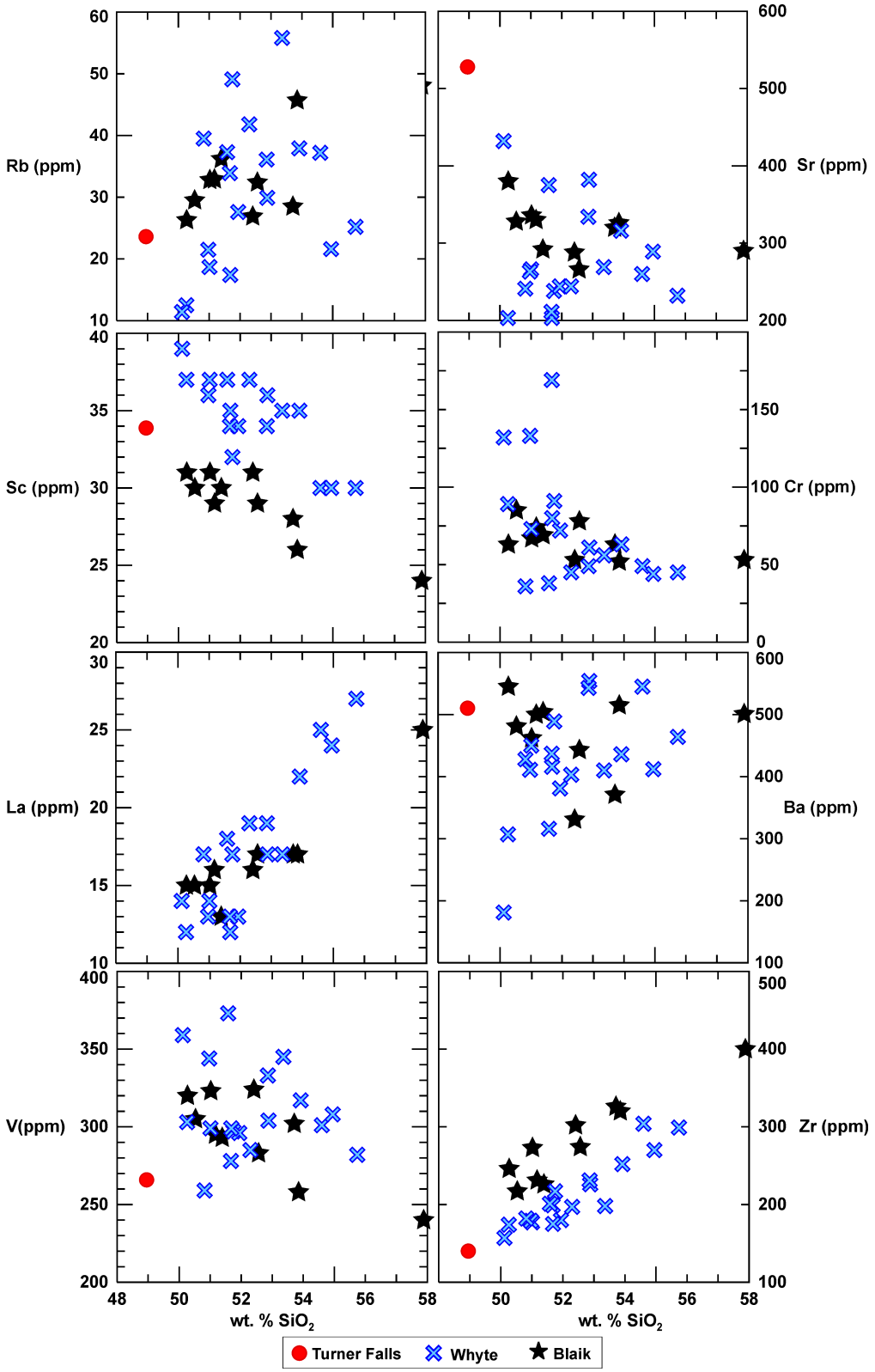

Figure 3.8 Harker diagrams showing concentrations of trace elements in ppm.

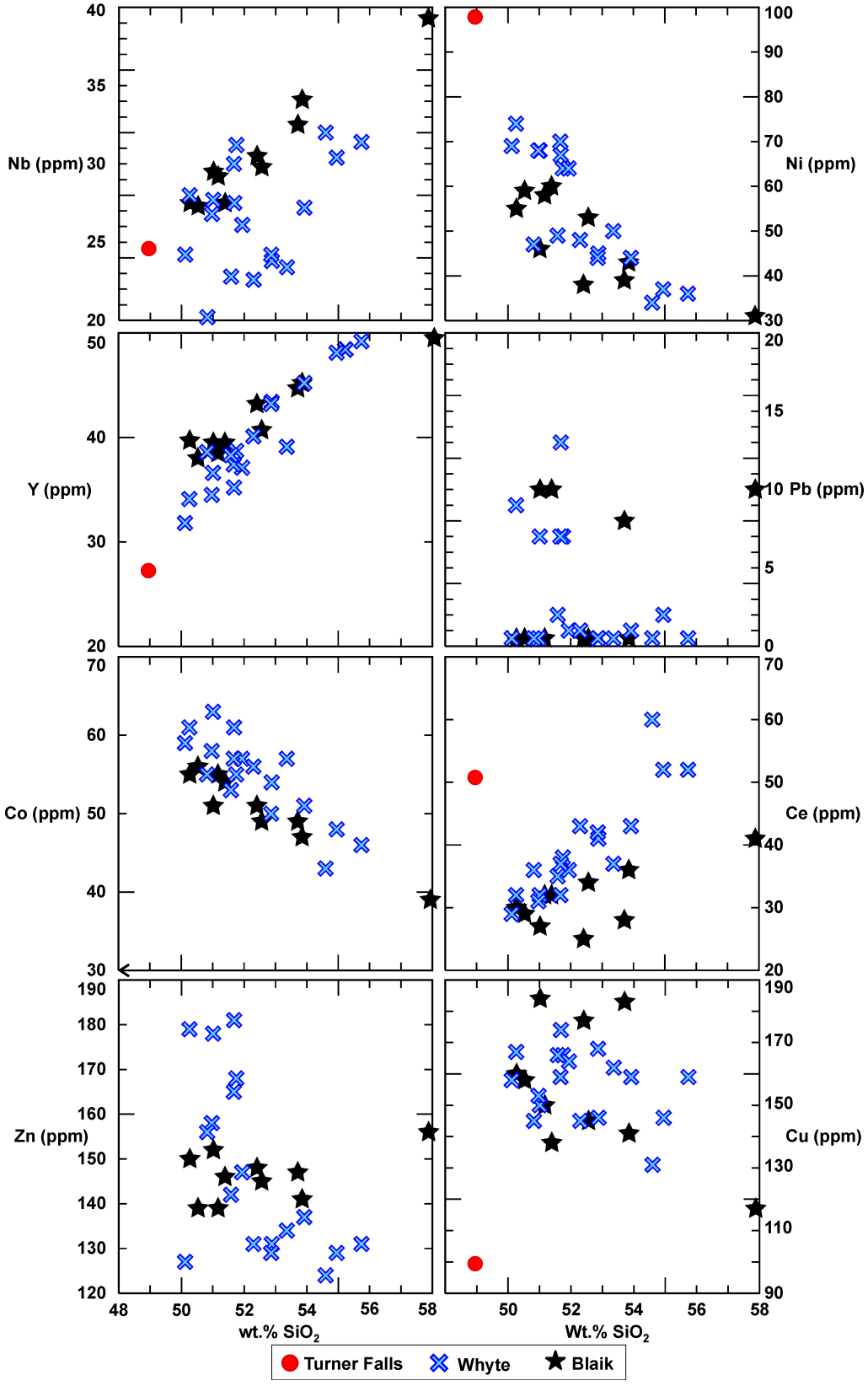

Figure 3.9 Harker diagrams showing concentrations of trace elements in ppm.

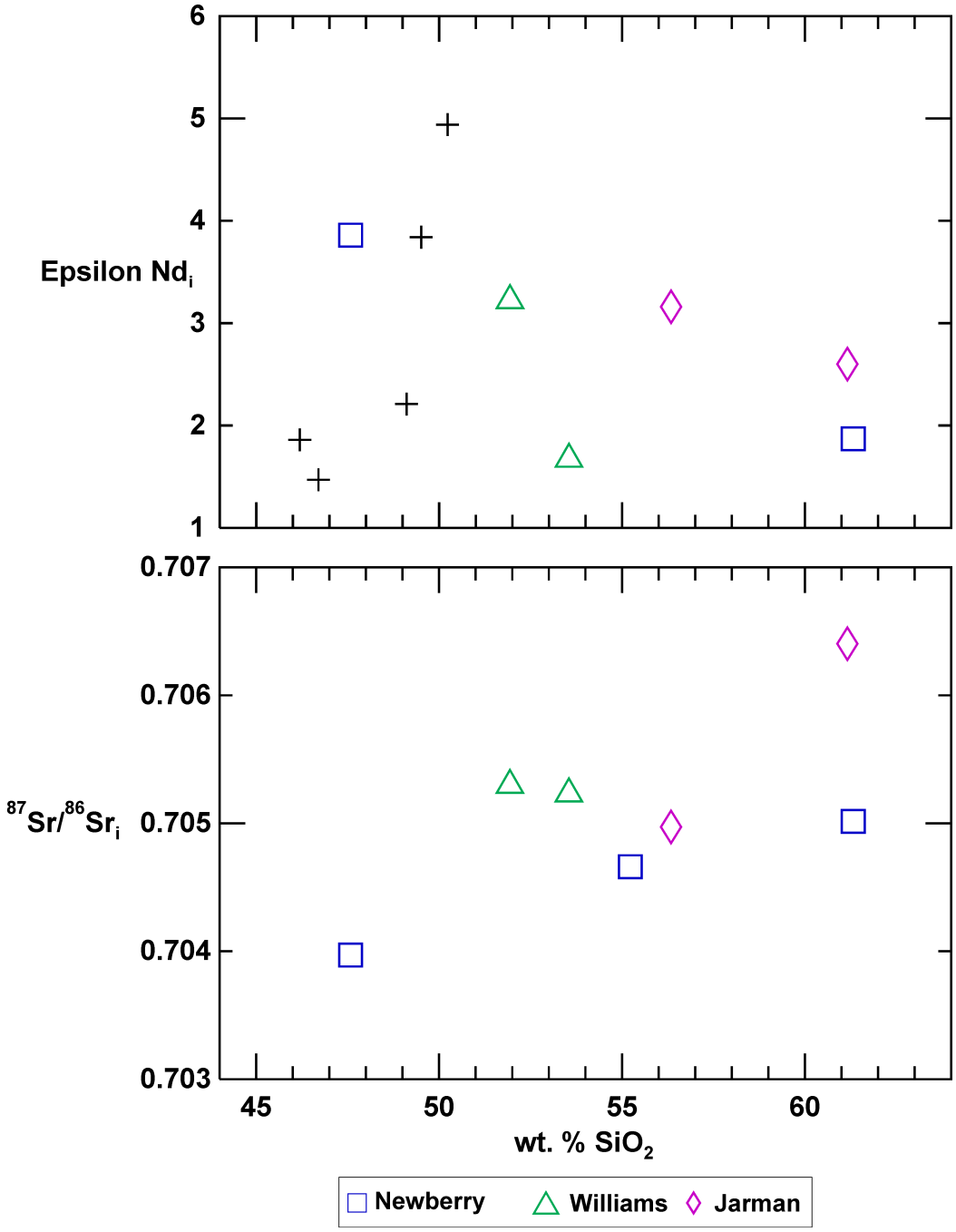

Figure 3.10 Isotope ratios vs wt.% SiO_2

Chapter 4 - Discussion

General Geochemistry

Many discrimination diagrams are useful in constraining the samples taken from the Arbuckle Mountains. By utilizing these diagrams, it can be inferred whether magma originated from hotspot volcanism, subduction, or adiabatic decompression-induced melting associated with a mid-ocean ridge. These diagrams also give insight into the location of the volcanic event: whether it was intraplate volcanism or occurred at a plate boundary.

When plotted on a MORB-normalized multi-element diagram the samples show enrichment in incompatible trace elements (Figure 4.1). This supports earlier interpretations that the rocks in the SOA are associated with LIP volcanism. The trend shown on the diagram is consistent with OIB volcanism, which would be enriched in melt-preferring elements compared to depleted MORB. Each well sampled has higher Ba with relation to other LILE. According to Weaver (1991), this is common in EM1 OIB. On a primitive mantle-normalized multi-element diagram (Sun and McDonough, 1989; Figure 4.2), the samples show similar trends to OIB lavas, primarily a high ratio of large ion lithophile elements (LILE) to light rare earth elements (LREE). This too is an expected trend with EMI OIB's, as is a relative decrease in heavy rare earth elements (HREE).

On the tectonic discrimination diagram by Meschede (1986), the samples plot as intraplate tholeiitic basalts (Figure 4.4). On the discrimination diagram used by Pearce and Cann (1973), the samples plot as intraplate basalts and calc-alkaline basalts (Figure 4.5). Figure 4.6 shows the samples plotted on the discrimination diagram of Mullen (1983). On this diagram the samples from the Blaik and Turner Falls well plot as OIB, while the Whyte well samples plot

along the border of OIB, MORB, and IAB. Overall, the samples from these wells show a general geochemical representation of intraplate tholeiitic basalts to andesites, which is supportive of the hypothesis that the LIP volcanism in the Arbuckle Mountains is evidence of a flood basalt event.

Relationship to Other Arbuckle Samples

In this section, the samples from this study are compared to other samples from the Arbuckle Mountains: extrusive basalts to andesites previously analyzed by Bulen (2012) and mafic dikes studied by Lidiak et al. (2014). The extrusives studied by Bulen (2012) are believed to be of the same magmatic event as those first analyzed in this study. The dikes are believed to have formed during the eruption process that created the LIP. The samples analyzed by Bulen (2012) come from three wells within the SOA. They are located along strike with the three wells analyzed in this study, northwest of the Turner Falls well and southeast of the Blaik and Whyte wells (Figure 2.1). The 48 samples plot as tholeiitic basalts to andesites, and as intraplate OIB lavas (Bulen, 2012). Along with the samples in this study, the complete analysis of the extrusives gives a fuller representation of the geochemistry of the SOA and from here on, the analysis of the extrusives will include all six wells.

When all the samples are plotted on the total alkalis and silica diagram of Lebas et al. (1986), the entire Arbuckle suite plot as tholeiitic basalts to andesites and trachybasalts to trachyandesites. The samples contain a wide spread of 47 to 63 wt. % SiO_2, of which the majority are below 55 wt. % SiO_2. Samples from Pan-Am Jarman range from 55 to 63 wt.% SiO_2. Samples from Pan-Am Williams range from 52 to 60 wt.% SiO_2. Samples from the Pan-Am Newberry have a much broader range, from 47 to 62 wt.% SiO_2. With increasing SiO_2 the samples decrease in wt. % MgO, CaO, FeO and Fe_2O_3. The samples also increase in wt. %Na_2O,

and K_2O. Samples decrease in Sr, Ni, V, and Sc, and they increase in Rb, Zr, La, Ba with increasing wt. % SiO_2, consistent with fractional crystallization.

There is a clear distinction between low TiO_2 and high TiO_2 samples within this study. A gap appears between those of the Blaik and Newberry wells, and those of the Turner Falls, Whyte, and Williams wells. The Jarman well has samples on both sides of this split. Beccaluva et al., (2009) shows that a difference in TiO_2 in plume-related volcanism along a continental rift is evident of the location and depth of which the melting occurs. High TiO_2 lavas are believed to be representative of melts occurring at the center of a plume, from higher temperatures and depths, while low TiO_2 lavas would be representative of melts formed away from the center of the plume. Melting of these lavas would occur nearer to the surface, at lower temperature and pressure (Beccaluva et al., 2009). While there are variations in TiO_2 in the Arbuckle samples, both groups show trends similar to High TiO_2, transitional, tholeiites in Figure 4.3.

Lutinen et al. (2014), supports the results of Beccaluva et al. (2009), with regards to generation pressure of high and low TiO_2 melts. Lutinen et al. (2014) also propose, along with Gibson et al. (1995), that variations in TiO_2 would also be visible in certain trace element ratios. With the samples from the SOA, this is visible in Figure 4.7, Figure 4.11, and clearly in Figure 4.15, with the high Ti samples having higher Zr/Y and Zr/Nb, and lower La/Nb and K/P, while the low Ti samples have higher La/Nb and K/P, and lower Zr/Y and Zr/Nb. However, it is still somewhat unclear what process caused the TiO_2 difference, and both magma types show similar normalized trace element characteristics, which would not be expected if the TiO_2 differences reflect the role of different mantle sources involved in melting. Furthermore, overall, they have similarities that are comparable to an OIB-like mantle source that would be associated with hotspot volcanism and a large igneous province such as the SOA (Figure 4.16).

The diabase dikes from Lidiak et al. (2014) are geochemically more primitive than the other Arbuckle samples. These dikes have wt.% SiO_2 values lower than 52, and wt.% MgO values between 4.25 and 7.25. They have wt.% TiO_2 values ranging between 1.85 and 2.87, which falls between the sets of high and low TiO_2 variations seen in other Arbuckle samples (Figure 4.7). K/P values for the dikes are mostly under 5, which shows most are likely uncontaminated. La/Nb values for these samples plot between 0.9 and 1.1, staying within the accepted EMI values, as well as around the higher end of the other Arbuckle values. The majority of the Arbuckle dikes share a similar geochemistry to the Turner Falls well samples, and are by far the most primitive of the SOA samples.

The diabase dikes have $^{87}Sr/^{86}Sr$ values of 0.703918 to 0.704359 and $^{143}Nd/^{144}Nd$ values of 0.512028 to 0.512206, and epsilon Nd values of 2 to 5.1. These values fall within the lower boundaries of the accepted present day EMI isotope values of Zindler and Hart (1986), 0.7040 to 0.7055 for $^{87}Sr/^{86}Sr$, and 0.5120 to 0.5123 for $^{143}Nd/^{144}Nd$. These values are age corrected to 535 Ma, as are the samples analyzed for this study, and they all plot similarly (Figure 4.11). This provides more evidence that the collective geochemistry of the Arbuckle Mountains is that of a similar source and that the dikes represent possible conduits for the magma that eventually erupted at the surface. The hypothesis that the entire SOA LIP is one flood basalt event is supported by these data.

Relationship to Wichita Mountains

The Arbuckle Mountain samples are compared here to the Glen Mountain Layered Complex and the Roosevelt Gabbros of the Wichita Mountains. While data for these are scarce, some geochemical data from the Roosevelt Gabbros can be compared to the samples from the Arbuckles (Shapiro, 1981; Gilbert and Hughes, 1986). Roosevelt Gabbro outcrops can be seen

throughout the Wichita Mountains and may represent the intrusive component of the volcanism that produced the lavas associated with the potential flood basalt event proposed in this study. Sr and Nd isotope ratios from the Glen Mountain Layered Complex provides further insight into the similarities between the Wichita and Arbuckle Mountains within the SOA.

The Roosevelt Gabbros show similar geochemical trends to the samples from the Arbuckle Mountains (Figure 4.8). With increasing wt. % SiO_2, both show trends of decreasing MgO and increasing K_2O. The Roosevelt Gabbros tend to be more primitive, with generally higher wt. % MgO and lower wt. % K_2O. K/P and Zr/Nb ratios overlap those of the rocks from the Arbuckles. K/P values are generally lower than the Arbuckles (Figure 4.8).

Isotope ratios from the Glenn Mountains Layered Complex (GMLC) show similar $^{143}Nd/^{144}Nd$ values to those obtained from the Arbuckle Mountains, and slightly lower $^{87}Sr/^{86}Sr$ values when age corrected to 535 Ma (Lambert et al., 1988; Figure 4.11). $^{87}Sr/^{86}Sr$ values for the GMLC range from 0.703581 to 0.703616, $^{143}Nd/^{144}Nd$ values range from 0.512139 to 0.512703, and epsilon Nd values range from 3.63 to 5.27. There are a few possibilities to explain the lower $^{87}Sr/^{86}Sr$ values in the GMLC. This may be attributed to the intrusive formation of these samples, which may have involved significantly less mixing and contamination from the surrounding crust. They also may have erupted prior to the Arbuckle samples, representing an earlier glimpse into a less evolved magma chamber. It should also be noted that gabbros would have a lower concentration of Rb, a very incompatible element, and therefore less ^{87}Sr over time. The real reason is most likely a combination of the possibilities listed above.

The relationship between the Roosevelt Gabbros and the Arbuckle samples is one of the same magmatic event or of a very similar mantle source. The Roosevelt Gabbros are believed to represent the intrusive equal to the mafic-intermediate extrusives in the Arbuckles (Bulen, 2012).

However, new findings by Hogan and Amato (2015) show that the gabbros in the Wichita Mountains may be closer to 577 Ma. These findings show that instead of an intrusive equivalent, the gabbros may instead represent a separate, previous event that occurred before the Arbuckle eruptions, yet still one of a similar mantle source. Both the Arbuckle and Wichita Mountains are regarded as similar in tectonic setting, and are well understood to be a major part of the SOA LIP (Hanson et al., 2012; Puckett et al., 2014). Both the Roosevelt Gabbros, and the cuttings studied in this thesis, are interlayered with the Carlton Rhyolite, and follow the same SE-NW trend of the SOA.

Defining a Mantle Source

A mantle source for the magmas of the SOA can be inferred by using major element, trace element, and isotope ratios. A combination of these may provide insight into whether or not the SOA formed from an EMI, EMII, or HIMU mantle source. These ratios may also indicate whether or not the magmas that formed in this region were affected in any way from partial re-melting and contamination from the previously erupted crust.

Incompatible trace element ratios can give insight into the mantle reservoirs that act as the source rock for lavas. These ratios include Zr/Nb, La/Nb, Ba/Nb, K/Nb and Ba/Th. Ba/Nb and Ba/Th ratios may also act as indicators of a subduction zone environment. The incompatible trace element ratios of the samples most closely resemble those of Enriched Mantle Ocean-Island Basalts (EMI OIB, EMII OIB). EMI OIBs show evidence of recycled oceanic crust and pelagic sedimentary contamination, evident in high Ba, high U/Pb, and a relative depletion of HFSE. EMII OIB's show contamination of terrigenous sediment through low U/Pb and Rb/Sr ratios, low HFSE, as well as lower Ba concentrations than EMI OIB's (Weaver 1991, Stracke 2012). EMI OIB's show Zr/Nb values of 5 to 10, La/Nb values of 0.75 to 1.25, Ba/Nb values of 10 to

20, Ba/Th values of 80 to 150, and K/Nb values of 213 to 432 (Weaver, 1991). EMII OIB's have accepted values of 0.89 to 1.09 for La/Nb and 248-378 for K/Nb. These numbers overlap with the EMI values, while other ratios such as Ba/Nb, Ba/Th, and Ba/La are lower in EMII. Ba/Nb values for EMII range from 7.3-11.0 and Ba/Th values are 70-90.

The samples in this study show Zr/Nb values of 5.75 to 10.25, Ba/Nb values of 7 to 24. La/Nb values are 0.4 to 0.9 and overlap the lower end of the EM1 OIB range, while Zr/Nb and Ba/Nb match much better with a few outliers. The low Ba/Nb and Ba/Th concentrations also indicate a lack of subduction, which should be expected in the intraplate environment suggested by the discrimination diagram of Meschede (Figure 4.4). Figure 4.9 shows samples from the three wells in this project, as well as the samples analyzed by Bulen (2012) plotted for different trace element ratios. When compared to the averages for EMI, EMII, HIMU sources, as well as Upper Continental Crust (UCC), and Lower Continental Crust (LCC) averages, taken from Weaver (1991) and Rudnick and Gao (2003), the most primitive samples (< 53 wt. % SiO_2**)** show that the samples have characteristics similar to EMI OIB. K/Nb, Zr/Nb, and Ba/Nb ratios all plot closely around the accepted EMI values for the more primitive samples. Ratios such as La/Nb, Zr/Nb and Ba/Th have a little more diversity in their values. La/Nb and Zr/Nb show the potential for multiple arrays, split similarly to the variations seen with TiO_2. Ba/Th ratios are much more varied, with some nearing HIMU values. K/P, Zr/Y, and K_2O/MgO ratios show a slight trend towards upper crustal contamination. It's worth noting that while certain ratios have differing arrays, the differences are not split between the samples from Bulen (2012) and those first analyzed in this project. All of the wells studied here have similar geochemical traits, and while there is evidence to support multiple distinct lavas, all of the samples from the Arbuckle Mountains show trends similar to an EMI-type mantle source.

The Ba enrichment in relation to other LILE, and the high LILE/REE ratios is common in pelagic sediments and, as a result, EMI lavas. The Ba enrichment is not seen in EMII lavas or terrigenous sediments (Weaver 1991). With the addition of REE data, an enrichment of LREE compared to HREE can be seen (Figures 4.1, 4.2, 4.3**)**. High LREE/HFSE ratios and high LILE/REE ratios are also evident. Recycled oceanic crust, a component of OIB lavas, becomes dehydrated during subduction, depleting the crust of the more soluble LILE, and due to the mobility of the more incompatible trace elements and their likeliness to join the melted portion of the mantle, OIBs show high amounts of incompatible trace elements: LILE and to a lesser extent, LREE. These are elements that favor the melt over the solid, and will enrich a magmatic source that undergoes small degrees of partial melting. Due to the enrichment in the incompatible, highly mobile trace elements, OIB-type lavas are often depleted in immobile HREE compared to the somewhat mobile LREE and highly mobile LILE (Weaver, 1991). This is evident throughout the entire suite of samples, as the high and low TiO_2 lavas share similar OIB-like trends across LILE, LREE, and HREE on multi-element diagrams (Figure 4.16).

OIB sources also have distinct major element ratios, such as with CaO/Al_2O_3 and K_2O/TiO_2 (Jackson and Dasgupta, 2008). HIMU lavas have a high CaO/Al_2O_3 ratio and a low K_2O/TiO_2 ratio, while EM lavas have lower CaO/Al_2O_3 ratios and higher K_2O/TiO_2 ratios. Samples from the Arbuckles plot as 0.35 to 0.75 for CaO/Al_2O_3, which overlaps the range of EMI values for CaO/Al_2O_3 (0.5 to 0.6), but lower than the range of EMII values (0.85 to 0.95). The Arbuckle samples have a slightly higher range of K_2O/TiO_2 values than the accepted values of enriched mantle sources. This is probably due to crustal contamination, due to partial melting of the underlying crust in the SOA. These ratios may be seen in figure 4.10.

The hypothesis that the SOA is composed of lavas derived from an EMI-type source is further supported by the results of isotope data, which fall within the range of accepted EMI values for $^{87}Sr/^{86}Sr$, 0.7040 to 0.7055, and $^{143}Nd/^{144}Nd$ ratios, 0.5120 to 0.5123 (Figure 4.11). As noted previously, when age corrected to 535 Ma, all the samples from the SOA fall under similar Sr and Nd isotope ratios. This is further evidence towards the hypothesis that the aulacogen was formed by an EMI source in relation to flood basalt volcanism.

EMI and EMII lavas generally have a higher wt.% K_2O than HIMU lavas due to the addition of recycled crustal sediments. However, a higher K concentration is also evidence of crustal contamination. K/P, K/Nb, K_2O/MgO, and K_2O/TiO_2 ratios of SOA samples have higher than expected values for enriched mantle sources, staying between EMI and UCC values. This is consistent with a role for contamination from the local bedrock that predates the aulacogen, although this interpretation is only conjecture at this point, because adequate geochemical data aren't currently available for these rocks. Carlson and Hart (1987) state that a K/P ratio greater than 5 is an indicator of upper crustal contamination, and most of the samples from this study fit that description. Another example of crustal contamination comes from comparing Sr isotope ratios and K/P ratios (Figure 4.12). When plotted against SiO_2, both show similar trends, which is an indication of contamination in Sr values. In an ideal system, age-corrected Sr isotope values would not change with an increase in SiO_2. These values may also have been altered during the drilling process, during which fluids may have contaminated the samples. This may also provide an explanation for the low CaO and high Al_2O_3 samples from the Whyte well mentioned in Chapter 3. However, while there is an indication of contamination, sample CB-PAN-20 represents an unaltered, primitive view into the geochemistry of the Arbuckle Mountains. This sample is a basaltic tholeiite, with high MgO and low SiO_2, and a $^{87}Sr/^{86}Sr_i$ value of 0.703970

and an epsilon Nd value of 3.86, showing that there is clear evidence in major, trace, and isotope values to support that the SOA samples represent EMI-type lavas formed as part of a LIP.

Chemostratigraphy

Figure 4.13 shows chemostratigraphic variations in compositions of SiO_2, FeO*, Ni, Zr, and K/P for the Blaik and Whyte wells. Concentrations of SiO_2 and FeO* are used to show diversity in major elements, while Ni and Zr concentrations are used to show differences in compatible and incompatible trace elements. Throughout the chemostratigraphic figures, the y-axis stays constant while the x-axis will vary with the geochemical component. The only similarity in depth between mafic intervals in the two wells occurs around ~2000 m. This interval contains the most shallow of the Blaik well samples and the deepest of the Whyte well samples. These samples contain similar trace element concentrations, with nickel concentrations ranging around 30-60 ppm, and relatively low zirconium concentrations from 200-330 ppm. K/P values vary significantly, with Blaik well samples ranging from 6 to 10 with an outlier of 12, while the Whyte samples range from 4 to 16 regardless of depth, with an outlier of 19.

It is much easier to see potential flow packages between samples in the Whyte well than the Blaik well. Most of the samples in the Blaik are relatively primitive and there is not a large gap in depth between samples. With the Whyte well, there is a gap of roughly 200 meters between JH-14-29 and JH-14-31. This gap separates the samples into a shallow cluster (samples JH-14-23 through JH-14-29) and a deep cluster (samples JH-14-31 through JH-14-41). The shallow cluster samples tend to have similar geochemical traits, while the deep cluster samples show both similar traits and a broader range depending on the major or trace element. The shallow cluster of the Whyte well overlaps the most primitive compositions observed for

the the deep cluster: Zr concentrations between 175 and 225 ppm; Ni concentrations between 60 and 75 ppm; Y concentrations around 35 ppm; Co concentrations between 55 and 65 ppm; and La concentrations between 12 and 18 ppm; as well as major element concentrations of SiO_2 between 50 and 52 wt%; TiO_2 concentrations between 2.0 and 2.4 wt%; Al_2O_3 concentrations between 14 and 15 wt%; and MgO concentrations between 6.5 and 7.5 wt%. The deep cluster has localized concentrations in TiO_2, Al_2O_3, Ni, Cr, and Th. TiO_2 concentrations are between 1.6 and 1.9 wt%; Al_2O_3 concentrations are between 13 and 14 wt%; Ni concentrations are between 35 and 50 ppm; Cr concentrations are between 30 and 70 ppm; and Th concentrations are between 6 and 10 ppm (Figure 4.14).

Chemostratigraphy shows the possibility of different lava packages, some with varying geochemical signatures. However, due to differing depths of the extrusive samples found in the wells across the study area as well as the faulting and folding that has occurred in the SOA, it is not possible at this time to accurately outline the separate flows. It should be noted, however, that samples from the Whyte well trend less evolved towards the surface. This may represent a magma chamber refilling with new, primitive samples with time.

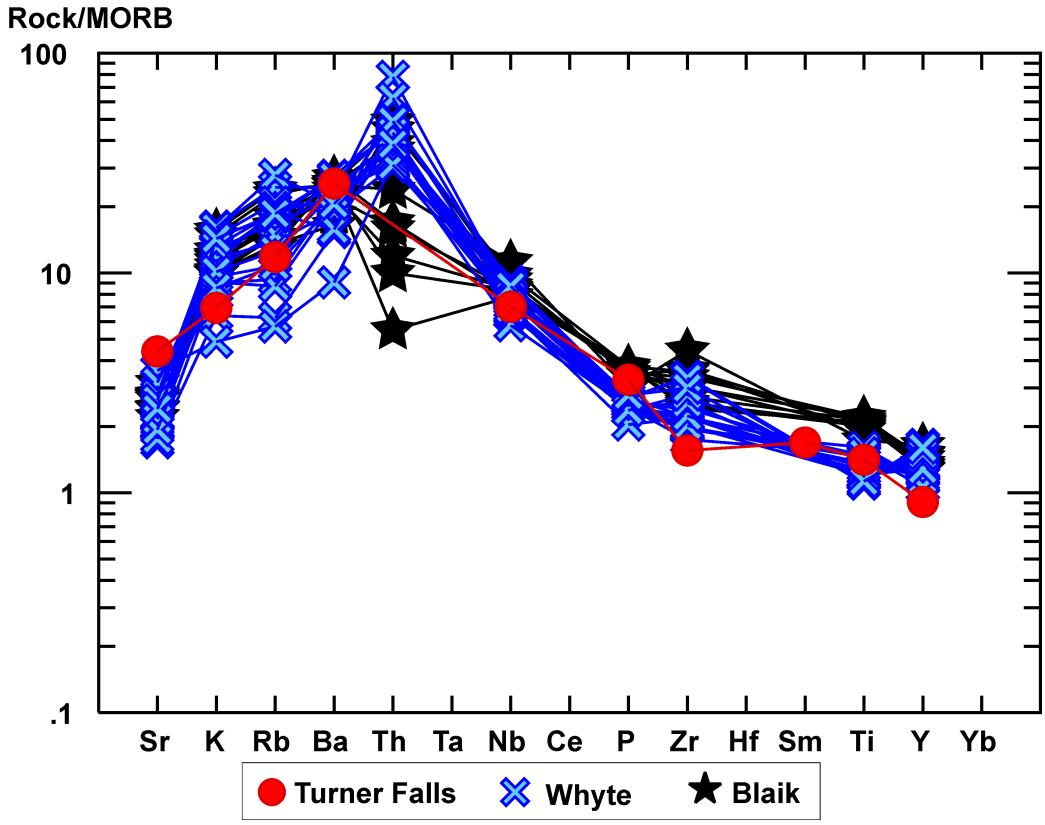

Figure 4.1 MORB-normalized spider diagram for the three wells studied in this thesis.

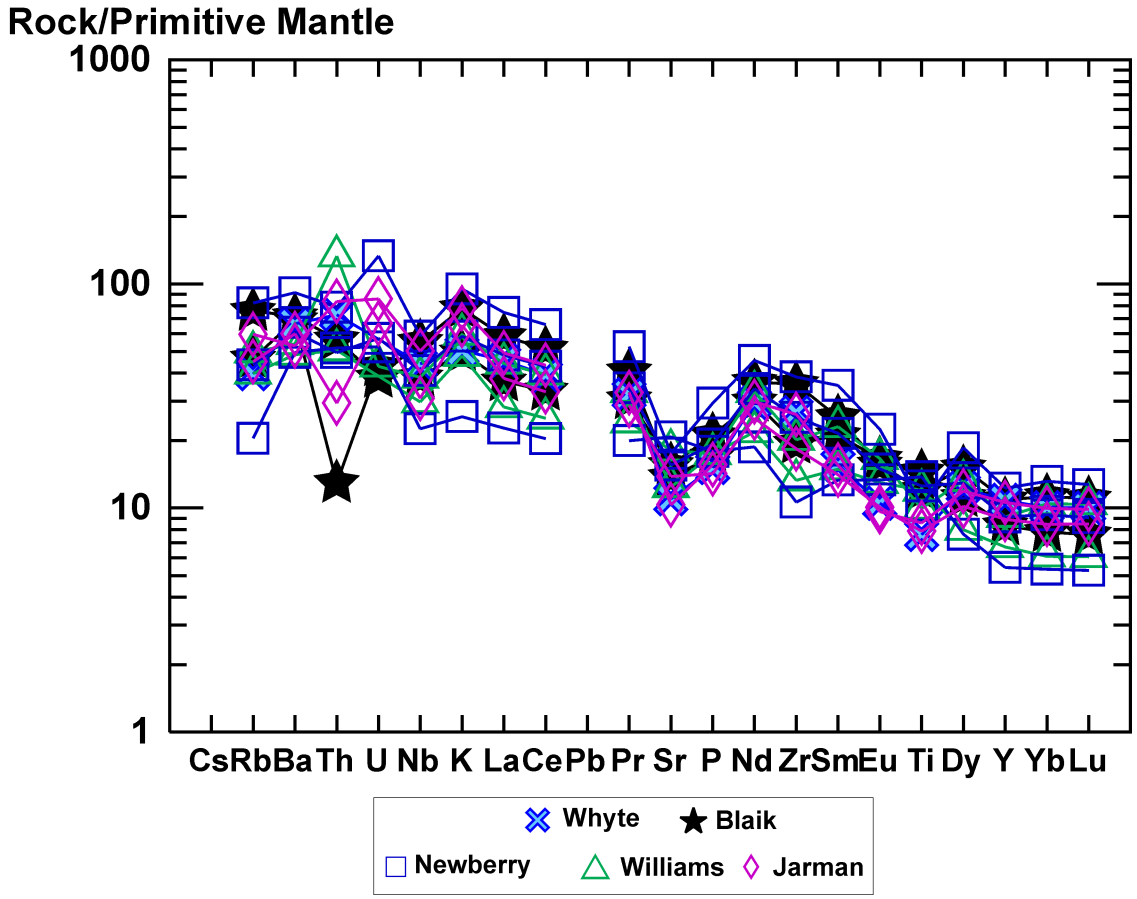

Figure 4.2 Primitive Mantle-normalized spider diagram for the ten samples that underwent REE analysis.

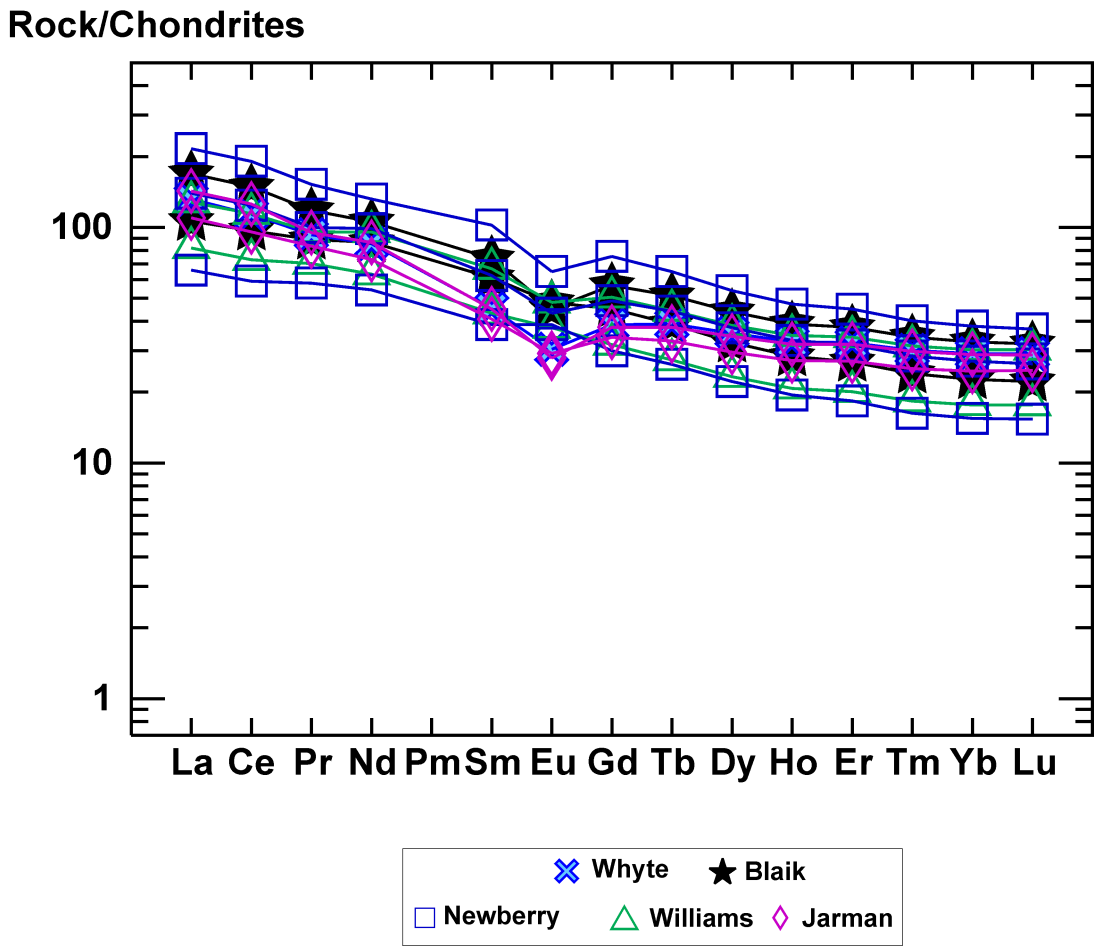

Figure 4.3 Chondrite-normalized spider diagram utilizing REEs. Ten samples from five wells were analyzed and are shown here.

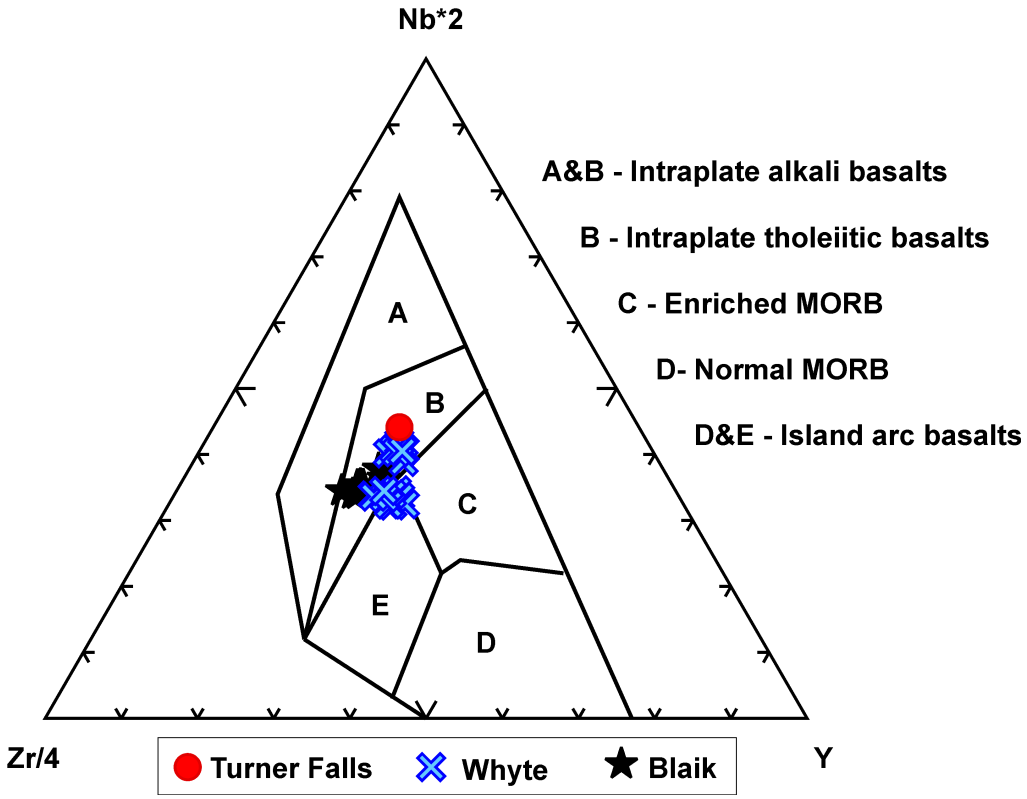

Figure 4.4 Discrimination diagram modified from Meschede (1983).
Utilizes incompatible trace elements to determine the plate tectonic setting associated with producing the samples.

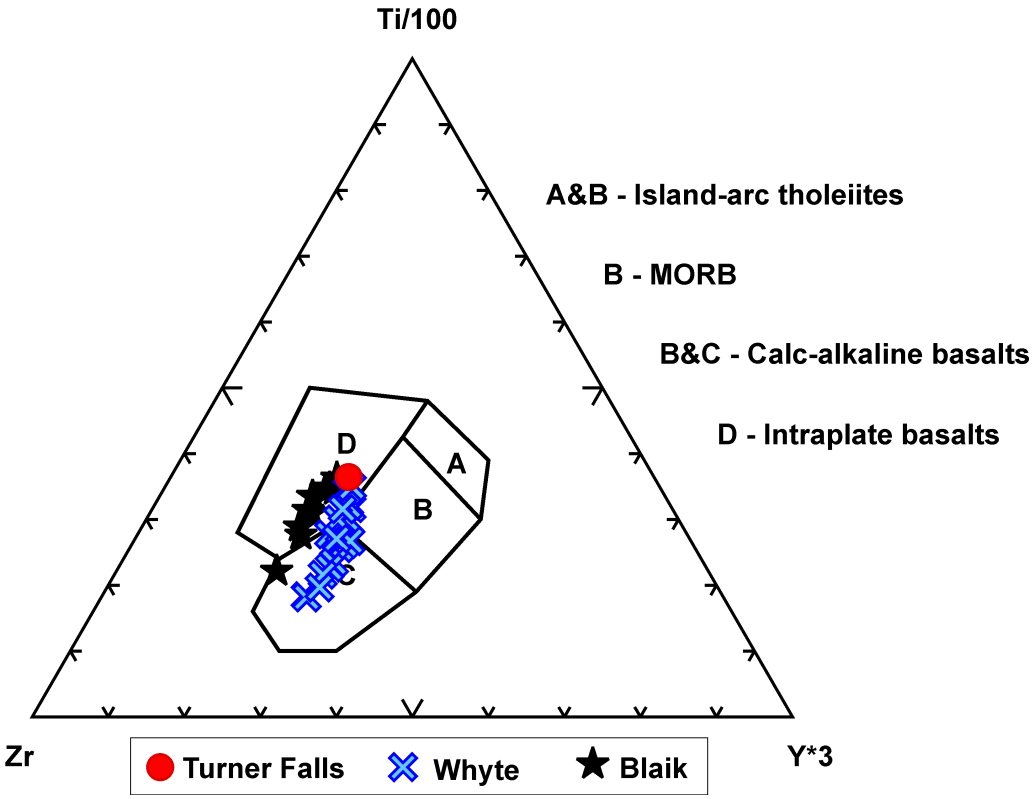

Figure 4.5 Discrimination diagram of Pearce and Cann (1973).
Utilizes Ti, Zr, and Y concentrations to distinguish between MORB, IAB, and OIB magmas.

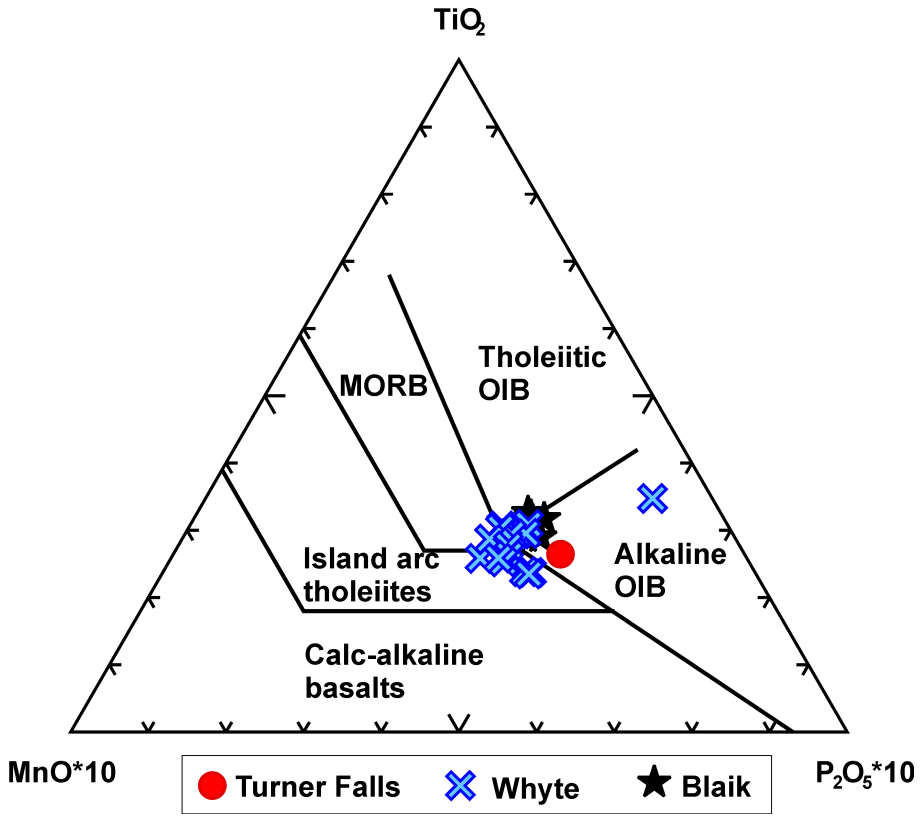

Figure 4.6 Discrimination diagram, modified from Mullen (1983).
Utilizes major element concentrations to distinguish between different tectonic settings.

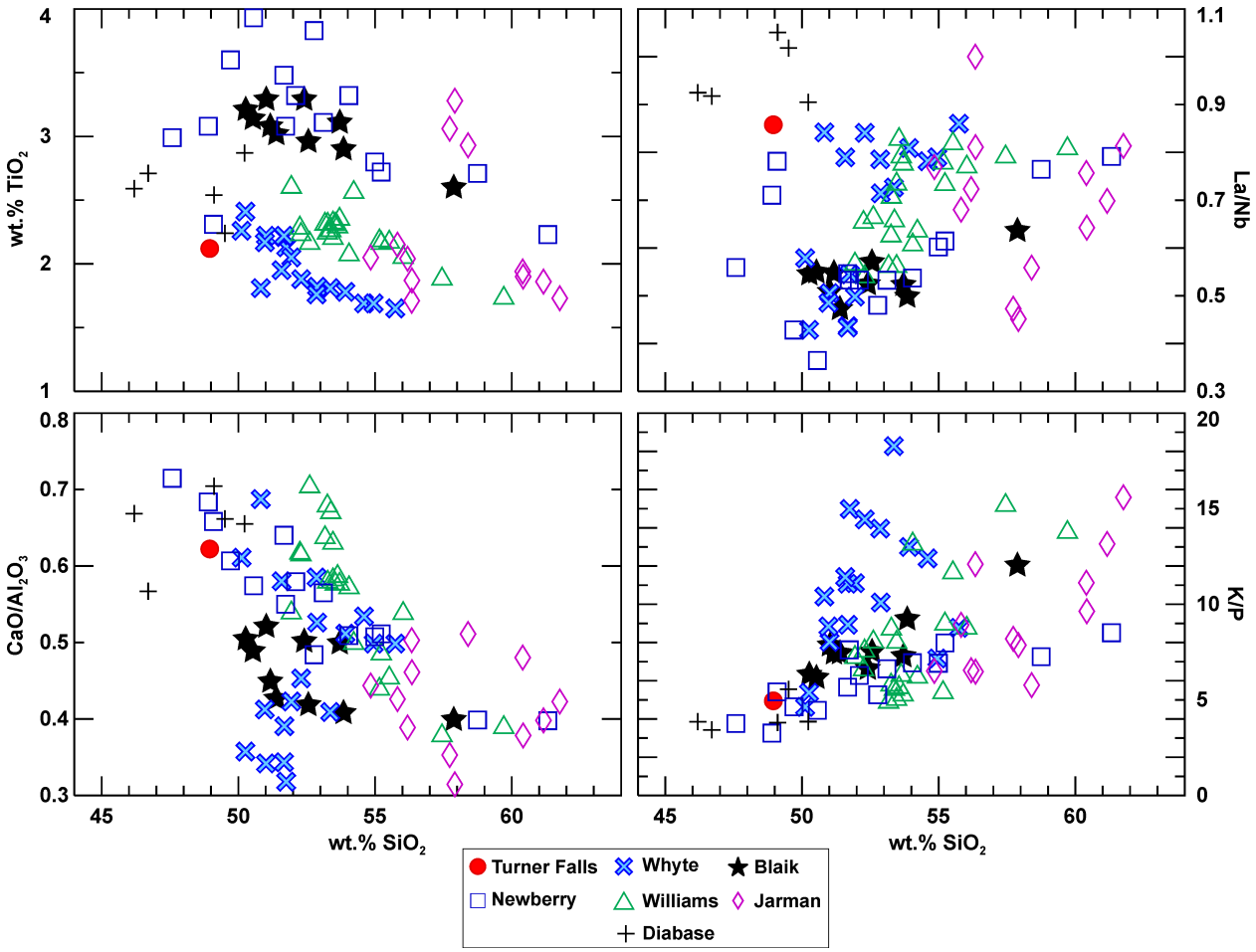

Figure 4.7 wt.% TiO_2, CaO/Al_2O_3, La/Nb, and K/P ratios vs. wt.% SiO_2.
The diabase dikes are from Lidiak et al. (2014).

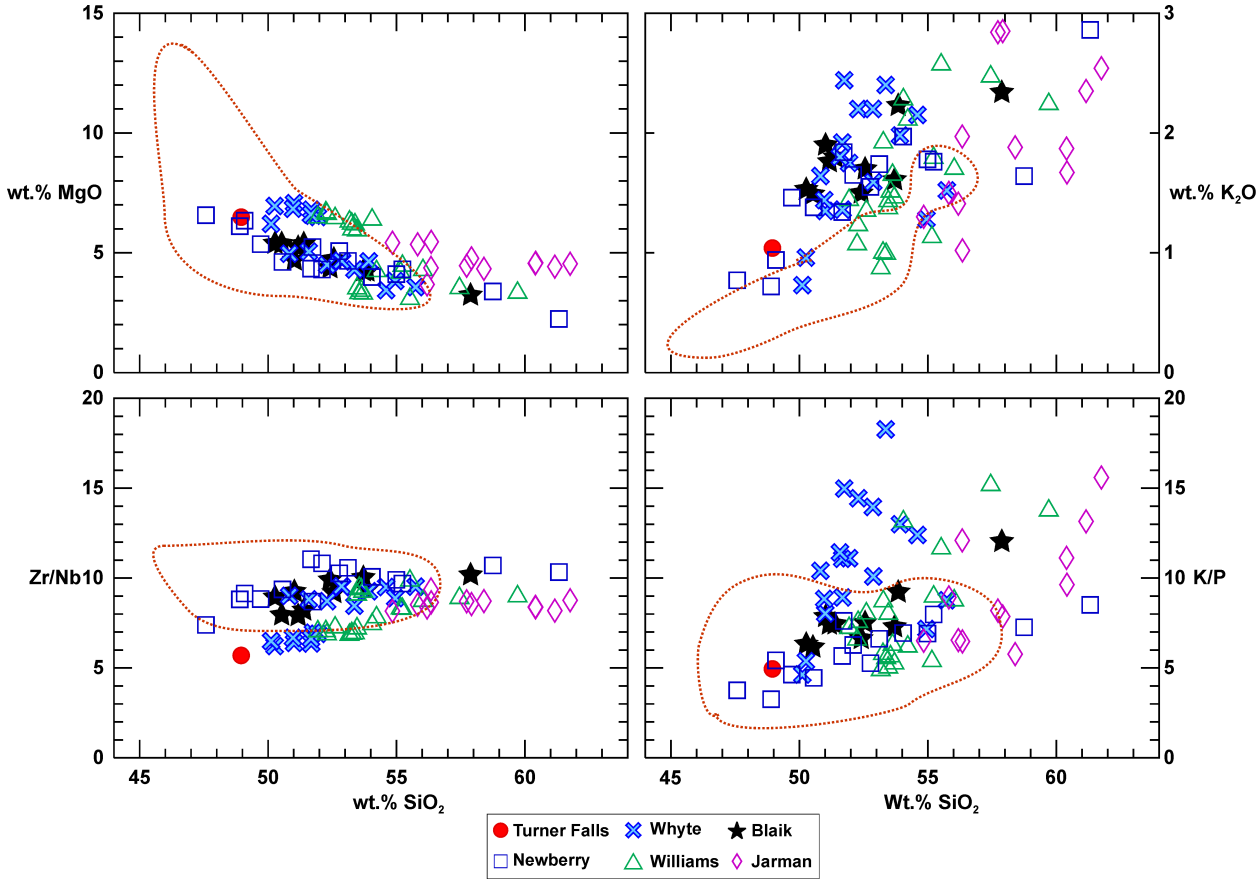

Figure 4.8 wt.% K_2O, wt.% MgO, Zr/Nb ratios, and K/P ratios vs. wt.% SiO_2

The dashed red line represents the Roosevelt Gabbros of the Wichita Mountains, from Shapiro (1981), Gilbert and Hughes (1986), and Aquilar (1988).

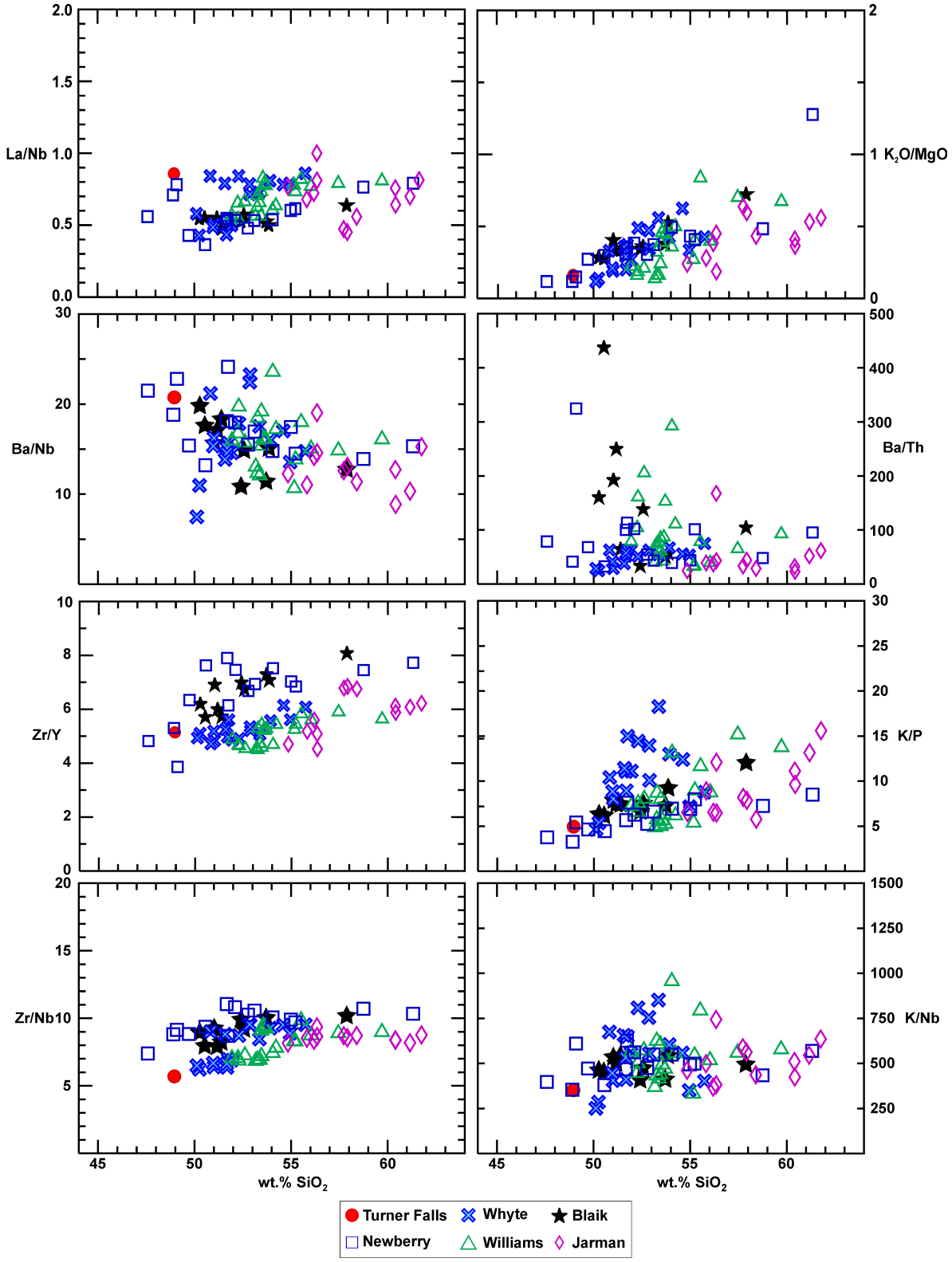

Figure 4.9 Incompatible major and trace element ratios versus wt. % silica.

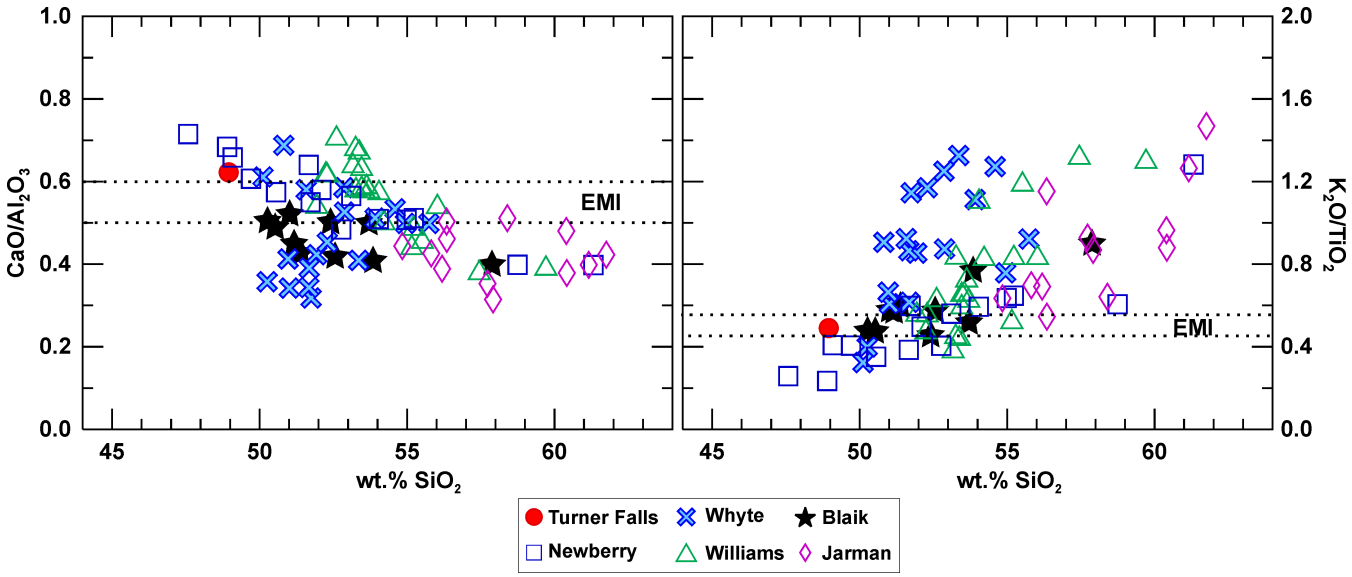

Figure 4.10 Major element ratios versus silica concentration (wt. %).
Major element ratios used here to further constrain these samples to an OIB mantle source. EMI values were taken from Jackson and Dasgupta (2008).

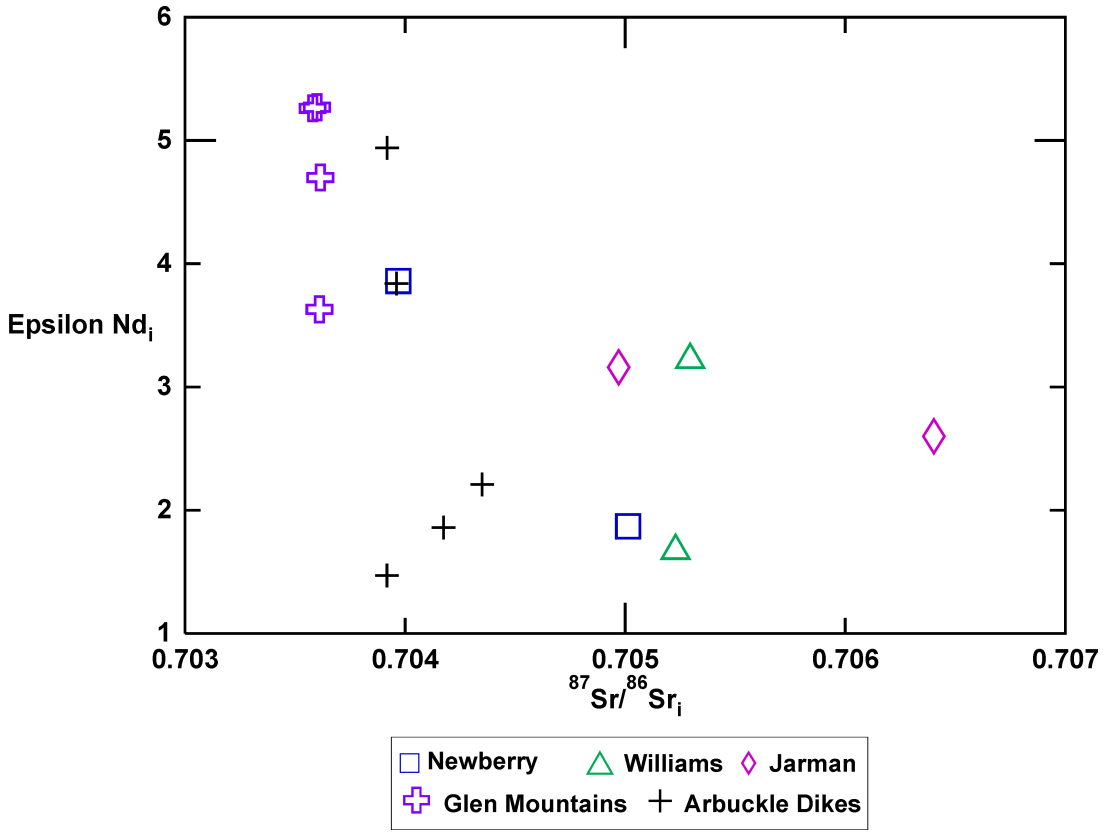

Figure 4.11 ^{87}Sr/^{86}Sr vs Epsilon Nd isotope ratios.

Used to constrain samples to a specific mantle source. Arbuckle dikes are from Lidiak et al. (2014), Glen Mountain samples are from Lambert et al. (1988).

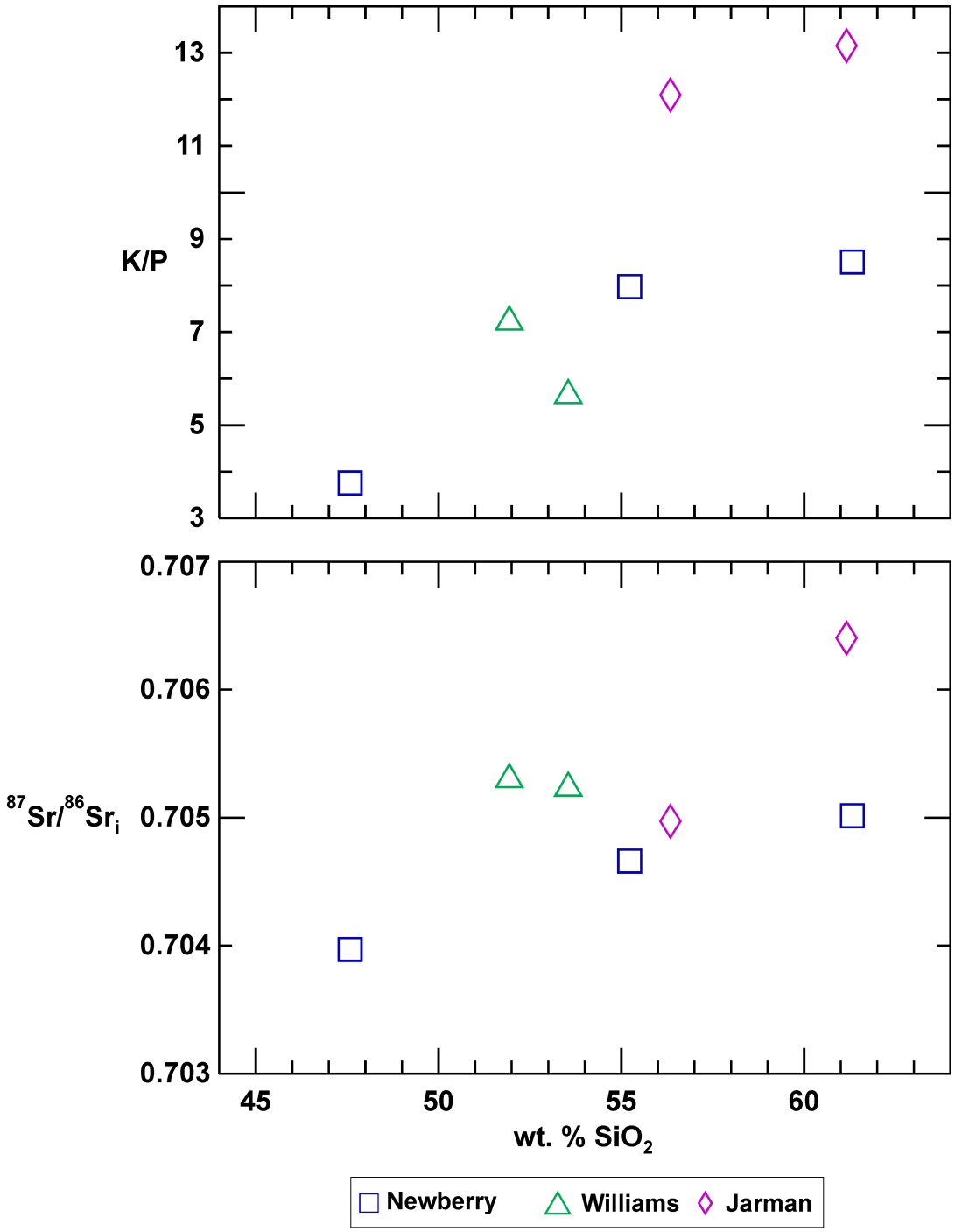

Figure 4.12 Sr isotope and K/P ratios vs wt.% SiO_2

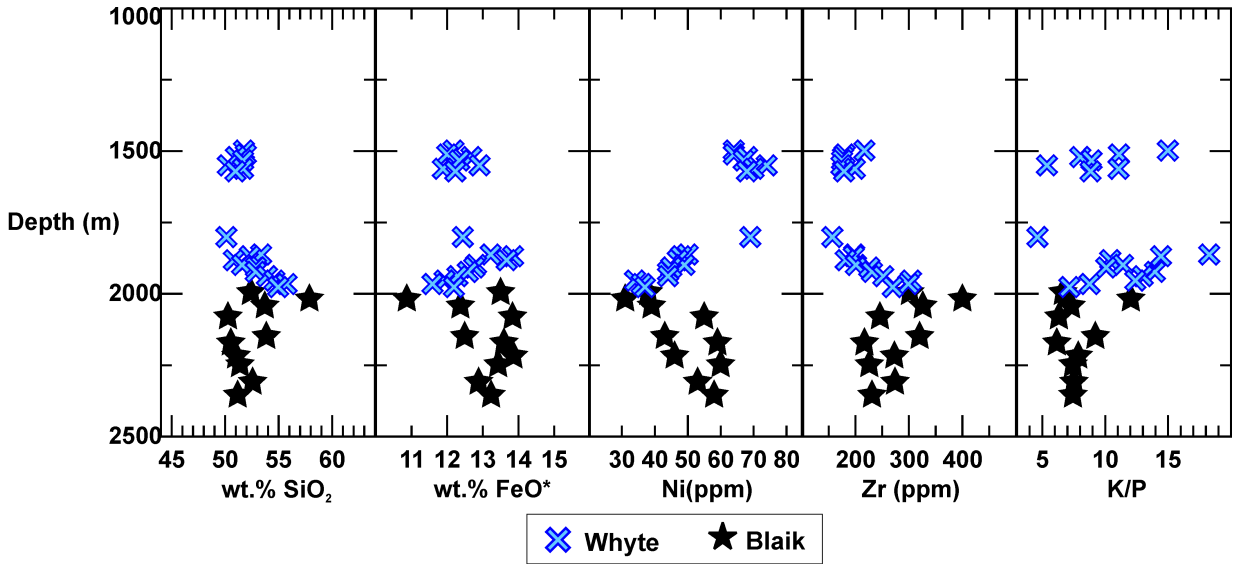

Figure 4.13 Chemostratigraphic diagrams depicting geochemical concentrations with depth.

Samples from two wells are plotted here. Major and trace elements were selected to show differences with depth.

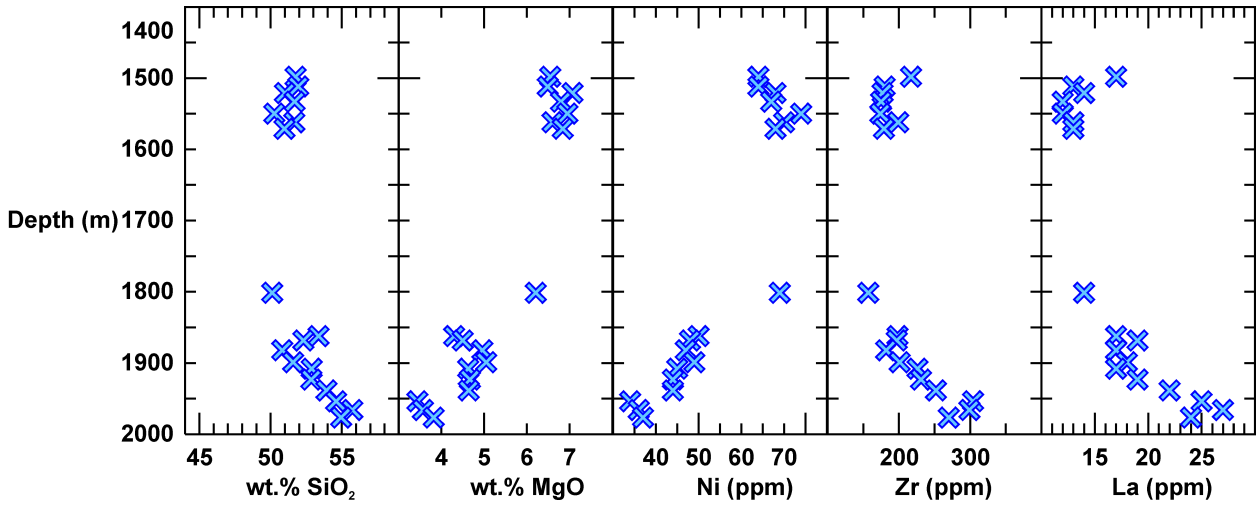

Figure 4.14 Chemostratigraphic diagrams depicting geochemical concentrations with depth.

Only samples from the Pan-Am Whyte well are shown in order to provide a better look at the differences in these samples with depth.

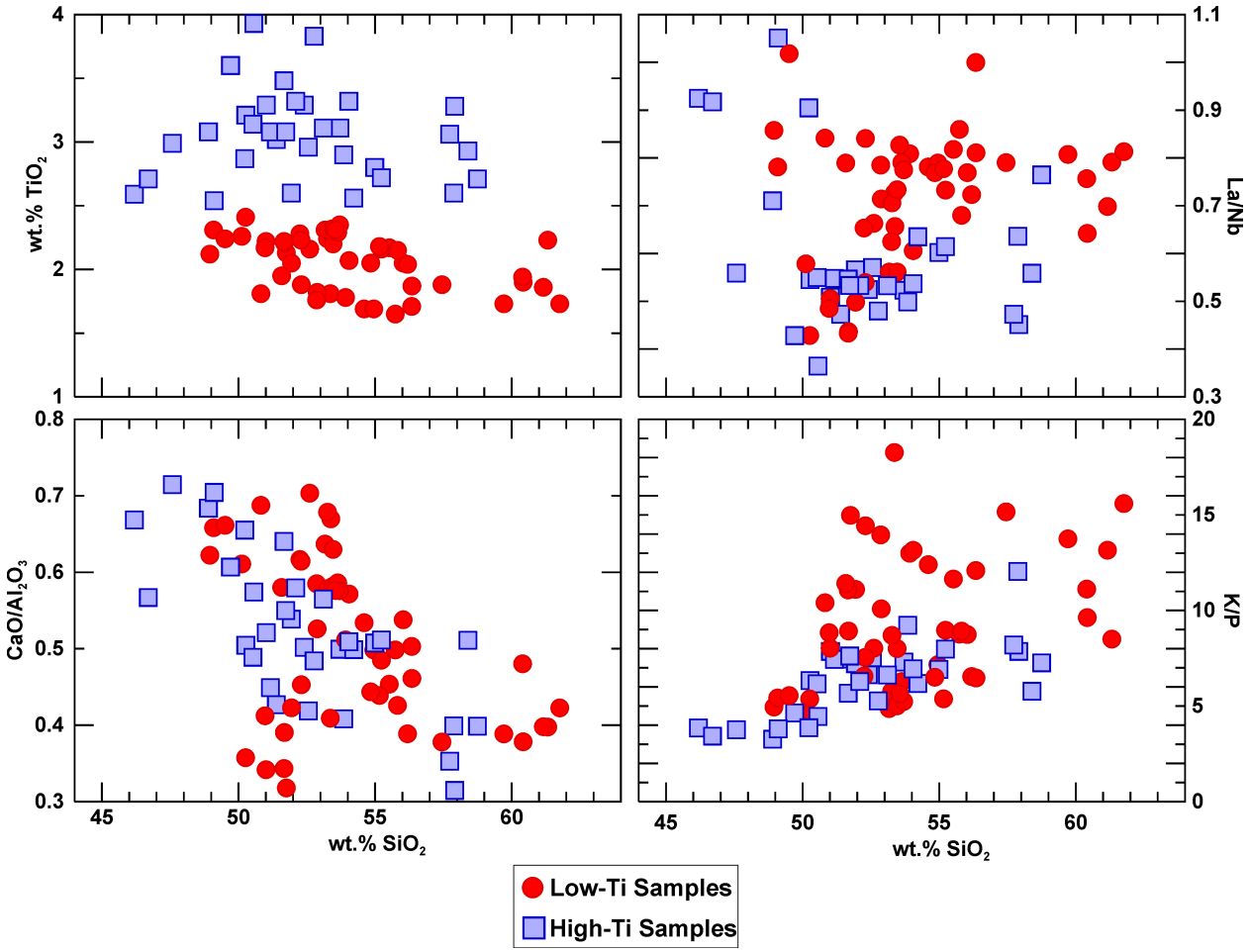

Figure 4.15 Titanium Variation in wt.% TiO_2, La/Nb, CaO/Al_2O_3, and K/P vs wt.% SiO_2 for samples from the Arbuckle Mountains.

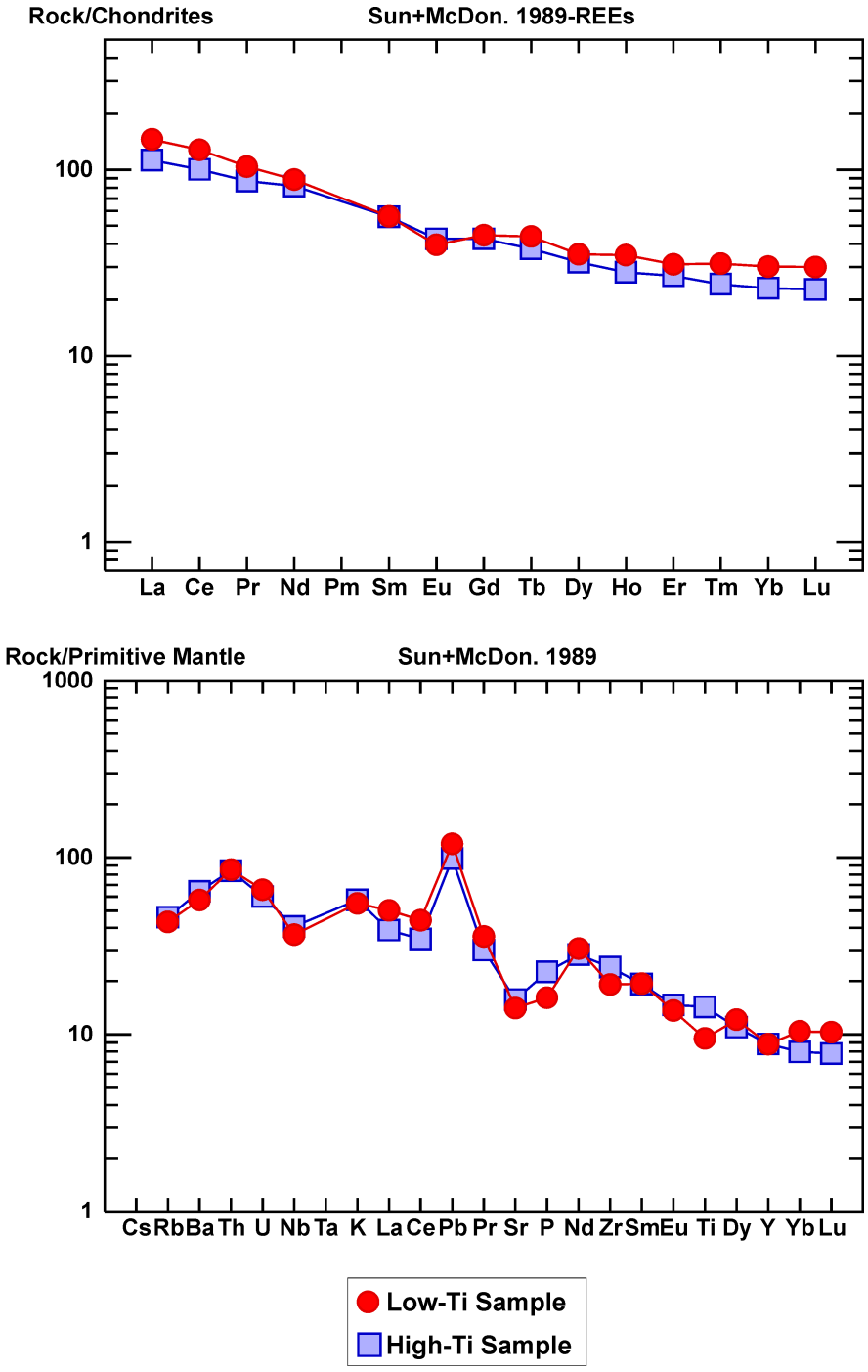

Figure 4.16 Chondrite and primitive mantle multi-element diagrams for high and low titanium averages.

Chapter 5 - Conclusions and Future Work

The Southern Oklahoma aulacogen represents an understudied large igneous province responsible for over 250,000 km^3 of mafic-felsic volcanism. The extent of the aulacogen strikes SE-NW through much of Oklahoma and into parts of northern New Mexico and Southern Colorado. Thanks to oil and gas exploration in the Arbuckle Mountains, Cambrian aged extrusive mafic-intermediate lavas were found and analyzed as a part of this study. These lavas represent the first evidence of extrusive mafic material in the Arbuckle Mountains. Prior to the extrusive mafic volcanism, only diabase dikes and the intrusive Roosevelt Gabbros of the Wichita Mountains provided evidence of mafic magmatism in the SOA.

These lavas can be defined as subalkaline to transitional tholeiitic basalts-andesites, and are representative of intraplate OIB volcanism. Based on the major element, trace element, and isotope chemistry, the Arbuckle samples are consistent with a substantial contribution of a mantle source enriched in recycled oceanic crust containing pelagic sediment (EMI OIB). Major element, trace element, and Sr and Nd isotope ratios for the SOA samples fall within and around the accepted EMI values. While evidence that the SOA formed from an EMI-type mantle source, it is also likely that some SOA magmas were affected by contamination from the upper continental crust.

This study argues that the SOA is not only an LIP, but is also representative of flood basalt volcanism. Flood basalts tend to be tholeiitic OIBs. They often erupt in multiple lava packages over a short period of time. Underneath the surface, there is often evidence of massive dike swarms and flood basalt events have been shown to be associated with rifting. The SOA fits each of these qualifications: samples plot as EMI OIB, chemostratigraphy shows the potential of multiple flow packages, crosscutting dike swarms are found in the subsurface of the aulacogen,

and while rifting in the SOA is associated with the opening of the Iapetus ocean, it could have been supplemented by the eruption of a flood basalt.

Future studies in the SOA should focus on obtaining isotope analyses on a larger suite of samples as well as obtaining precise dates for the lavas in the Arbuckle Mountains. In particular, samples of similar geochemistry to CB-PAN-20 would be ideal, as this sample is representative of the unaltered, uncontaminated source that formed the mafic-intermediate lavas in the aulacogen. This means studying low SiO_2, high MgO basaltic tholeiites, which fall in and around present day EMI OIB values. Obtaining precise dates on the lavas would also be beneficial, as this will confirm whether eruptions occurred in a timeframe accepted for flood basalt events, as well as providing a better understanding for the formation of the region in general.

References

Aquilar, J., 1988, Geochemistry of Mafic Rock Units of the Southern Oklahoma Aulacogen, Southwestern Oklahoma: *University of Oklahoma unpublished M.S. thesis*, 167 p.

Barry, T.L., Self, S., Kelley, S.P., Reidel, S., Hooper, P., and Widdowson, M., 2010, New $^{40}Ar/^{39}Ar$ dating of the Grande Ronde lavas, Columbia River Basalts, USA: Implications for duration of flood basalt eruption episodes: *Lithos*, v. 118, no. 3-4, p. 213-222.

Beccaluva, L., Bianchini, G., Natali, C., & Siena, F., 2000, Continental flood basalts and mantle plumes: a case study of the Northern Ethiopian Plateau. *Journal of Petrology*, 50(7), 1377-1403.

Beswick, A.E. and Soucie, G., 1978, A correction procedure for metasomatism in an Archean greenstone belt: *Precambrian Research*, v. 6, p. 235-248.

Bond, D. P., & Wignall, P. B., 2014, Large igneous provinces and mass extinctions: an update. *Geological Society of America Special Papers*, *505*, SPE505-02.

Brueseke, M. E., Bulen, C. L., and Mertzman, S. A., 2014, Major and Trace-element Constraints on Cambrian Basalt Volcanism in the Southern Oklahoma Aulacogen from Well Cuttings in the Arbuckle Mountains Region, Oklahoma (U.S.A.) *Oklahoma Geological Survey, Guidebook 38, p.95-104*

Bulen, C. L., 2012, The role of magmatism in the evolution of the Cambrian southern Oklahoma rift zone: geochemical constraints on the mafic-intermediate rocks in the Arbuckle Mountains, OK. *Kansas State University M.S. thesis.*

Cameron, M., Weaver, B.L., and Diez de Medina, D., 1986, A Preliminary Report on Trace Element Geochemistry of Mafic Igneous Rocks of the Southern Oklahoma Aulacogen *in* Gilbert, M.C., 1986, Petrology of the Cambrian Wichita Mountains Igneous Suite: *Oklahoma Geological Survey Guidebook*, v. 23, p. 80-85.

Carlson, R.W. and Hart, W.K., 1987, Crustal Genesis on the Oregon Plateau: *Journal of Geophysical Research*, v. 92, no. B7, p. 6191-6206.

Denison, R. E., Bickford, M. E., Lidiak, E. G., & Kisvarsanyi, E. B. (1987). Geology and geochronology of Precambrian rocks in the central interior region of the United States.

Eschberger, A.M., Hanson, R.E., and Puckett, R.E., 2014, Carlton Rhyolite Group and Diabase Intrusions in the East Timbered Hills, Arbuckle Mountains: *Oklahoma Geological Survey, Guidebook 38,* p. 143-186

Floyd, P.A. and Winchester, T.A., 1975, Magma type and tectonic setting discrimination using immobile elements: *Earth and Planetary Science Letters*, v. 27, no. 2, p. 211-218.

Gibson, S. A., Thompson, R. N., Dickin, A. P., & Leonardos, O. H. (1996). Erratum to "High-Ti and low-Ti mafic potassic magmas: Key to plume—lithosphere interactions and continental flood-basalt genesis"[Earth Planet. Sci. Lett. 136 (1995) 149–165]. *Earth and Planetary Science Letters*, *141*(1), 325-341.

Gilbert, M.C. and Hughes, S.S., 1986, Partial Chemical Characterization of Cambrian Basaltic Liquids of the Southern Oklahoma Aulacogen *in* Gilbert, M.C., 1986, Petrology of the

Cambrian Wichita Mountains Igneous Suite: *Oklahoma Geological Survey Guidebook*, v. 23, p. 73-79.

Hamilton, M., Elmore, R.D., Weaver, B., and Dulin, S., 2014, Petrology and Paleomagmatism of the Long Mountain Granite, Wichita Mountains, Oklahoma: *Oklahoma Geological Survey, Guidebook 38, p. 319-326*

Hanson, R.E. and Al-Shaieb, Z., 1980, Voluminous subalkaline silicic magmas related to intracontinental rifting in the southern Oklahoma aulacogen: *Geology*, v. 8, p. 180-184.

Hanson, R.E., Puckett Jr., R.E., Keller, G.R., Brueseke, M.E., Bulen, C.L., Mertzman, S.A., Finegan, S.A., and McCleery, D.A., Intraplate magmatism related to opening of the southern Iapetus Ocean: Cambrian Wichita igneous province in the Southern Oklahoma rift zone: *Lithos (2012)*

Hanson, R.E., and Eschberger, A.M., 2014, An Overview of the Carlton Rhyolite Group: Cambrian A-type Felsic Volcanism in the Southern Oklahoma Aulacogen: *Oklahoma Geological Survey, Guidebook 38,* p.123-142.

Hanson, R.E., Burkholder, B.K., Donovon, R.N., Dart, J.C., Frazier, S.J., McCleery, D.A., Phillips, C.M., and Pollard, J.B., 2014, Physical Volcanology and Geochemistry of the Carlton Rhyolite in the Slick Hills, Wichita Mountains: *Oklahoma Geological Survey, Guidebook 38,* p. 255-298.

Hofmann, A. W. (1997). Mantle geochemistry: the message from oceanic volcanism: *Nature*, *385*(6613), 219-229.

Hoffman, P., Dewey, J.F., and Burke, K., 1974, Aulacogens and their Genetic Relation to Geosynclines, with a Proterozoic Example from Great Slave Lake, Canada *in* Dott Jr, R.H. and Shaver, R.H., 1974, Modern and Ancient Geosynclinal Sedimentation: *SEPM Special Publication*, v. 19, p. 38-55.

Hogan, J.P., and Amato, J.M., 2015, Confirmation of Temporally Distinct Magmatic Events in the Wichita Mountains, Oklahoma: *Presented at the Geological Society of America South Central Section Meeting*.

Hooper, P.R., 2000, Chemical discrimination of Columbia River basalt flows: *Geochemistry, Geophysics, Geosystems*, v. 1, no. 1, p. 1024-1038.

Irvine, T.N. and Baragar, W.R.A., 1971, A Guide to the Chemical Classification of the Common Volcanic Rocks: *Canadian Journal of Earth Sciences*, v. 8, no. 5, p. 523-548.

Jackson, M. G., & Dasgupta, R., 2008, Compositions of HIMU, EM1, and EM2 from Global Trends Between Radiogenic Isotopes and Major Elements in Ocean Island Basalts: *Earth and Planetary Science Letters*, *276*(1), 175-186.

Keller, G.R. and Stephenson, R.A., 2007, The Southern Oklahoma and Dniepr-Donets aulacogens: A comparative analysis, *in* Hatcher, R.D., Jr., Carlson, M.P., McBride, J.H., and Martinez Catalan, J.R. (eds.), 4-D Framework of Continental Crust: *Geological Society of America Memoir*, v. 200, p. 127-143.

Krogh, T.E., 1982, Improved accuracy of U-Pb ages by the creation of more concordant systems using an air abrasion technique. Geochimica et Cosmochimica Acta, v. 46, p. 637-649.

Le Bas, M.J., Le Maitre, R.W., Streckeiser, A., and Zanettin, B., 1986, Chemical classification of volcanic rocks based on total alkali-silica diagram: *Journal of Petrology*, v. 27, no. 3, p.745-750.

Luttinen, A.V., Turunen, S.T., and Heinonen, J.S., 2014, Tracing Peridotite and Pyroxenite Sources of Karoo Flood Basalts in the Tete Province, Mozambique: *Presented at the California Goldschmidt Conference*.

LeMaitre RW (1976) The chemical variability of some common igneous rocks. J Petrol 17:589–637

Lidiak, E.G., Denison, R.E., and Stern, R.J., 2014, Cambrian (?) Mill Creek Diabase Dike Swarm, Eastern Arbuckles: A Glimpse of Cambrian Rifting in the Southern Oklahoma Aulacogen, *Oklahoma Geological Survey, Guidebook 38,* p. 105-122.

McConnell, D.A. and Gilbert, M.C., 1990, Cambrian extensional tectonics and magmatism within the Southern Oklahoma Aulacogen *in* Lucchitta, I. and Morgan, P. (eds.), Heat and Detachment in Continental Extension: *Tectonophysics*, v. 174, p. 147-157.

Mertzman, S.A., 2000, K-Ar results from the southern Oregon-northern California Cascade Range: *Oregon Geology*, v. 62, no. 4, p. 99-122

Mertzman, S.A., 2012, X-ray Laboratory. *Franklin & Marshall College Department of Earth and Environment*. Retrieved 2012, from http://www.fandm.edu/earth-and-environment/x- ray-laboratory.

Meschede, M., 1986, A method of discriminating between different types of mid-ocean ridge basalts and continental tholeiites with the Nb-Zr-Y diagram: *Chemical Geology*, v. 56, no. 3-4, p. 207-218.

Miyashiro, A., 1974, Volcanic rock series in island arcs and active continental margins: *American Journal of Science*, v. 274, p. 321-355.

Mullen, E.D., 1983, $MnO/TiO_2/P_2O_5$: a minor element discriminant for basaltic rocks of oceanic environments and its implications for petrogenesis: *Earth and Planetary Science Letters*, v. 62, no. 1, p. 53-62.

Pearce, J. A., 1982, Trace element characteristics of lavas from destructive plate boundaries: *Andesites*, 525-548.

Pearce, J.A. and Cann, J.R., 1973, Tectonic setting of basic volcanic rocks determined using trace element analyses: *Earth and Planetary Science Letters*, v. 19, no. 2, p. 290-300.

Patchett, P.J., and Ruiz, J., 1987, Nd isotopic ages of crust formation and metamorphism in the Precambrian of eastern and southern Mexico. *Contributions to Mineralogy and Petrology*, v. 96, p. 523-528.

Puckett, R.E., 2011, A thick sequence of rift-related basalts in the Arbuckle Mountains, Oklahoma, as revealed by deep drilling: *Shale Shaker*, Jan/Feb 2011, p. 207-216.

Puckett, R.E., Hanson, R.E., Eschberger, A.M., Brueseke, M.E., Bulen, C.L., and Price, J.D., 2014, New Insight into the Early Cambrian Igneous and Sedimentary History of the Arbuckle Mountains Area of the Southern Oklahoma Aulacogen from Basement Well Penetration: *Oklahoma Geological Survey, Guidebook 38,* p. 61-94.

Rudnick, R.L. and Gao, S., 2003, Composition of the Continental Crust *in* Holland, H.D. and Turekian, K.K. (eds), Treatise on Geochemistry, v. 3, no. 1, p. 1-64.

Shapiro, B.E., 1981, Chemistry and Petrography of the Navajoe Mountain Basalt Spillites of Southern Oklahoma: *University of Texas at Arlington unpublished M.S. thesis*, 116 p.

Stracke, A., 2012. Earth's heterogeneous mantle: A product of convection-driven interaction between crust and mantle. *Chemical Geology*, 330, 274-299.

Sun, S. S., & McDonough, W. F., 1989, Chemical and isotopic systematics of oceanic basalts: implications for mantle composition and processes: *Geological Society, London, Special Publications*, *42*(1), 313-345.

Thomas, W.A., 2006, Tectonic inheritance at a continental margin: *GSA Today*, v. 16, no. 2, p. 4-11.

Thomas, W.A., 2014, The Southern Oklahoma Transform-Parallel Intracratonic Fault System: *Oklahoma Geological Survey, Guidebook 38,* p. 375-388.

Walker, G. P., 1993, Basaltic-Volcano Systems: *Geological Society, London, Special Publications*, *76*(1), 3-38.

Weaver, B.L., 1991, The origin of ocean island basalt end-member compositions: trace element and isotopic constraints: *Earth and Planetary Science Letters*, v. 104, p. 381-397.

Winchester, T.A. and Floyd, P.A., 1977, Geochemical discrimination of different magma series and their differentiation products using immobile elements: *Chemical Geology*, v. 20, p. 325-343.

Zindler, A., & Hart, S., 1986, Chemical Geodynamics: *Annual review of earth and planetary sciences*, *14*, 493-571.

Appendix A - Arbuckle Samples

The table below shows the list of samples collected from the Oklahoma Petroleum Information Center, which is operated by the Oklahoma Geological Survey in Norman, Oklahoma. Listed are the sample names used throughout this thesis, as well as the corresponding well and depth from which the original well cuttings were obtained. Samples with a "*" were not discussed in this study due to high levels of alteration.

Sample	Well	Latitude	Longitude	Depth (ft).	Depth (m)
JH14-11	Blaik	34.56321	-97.50825	6545	1994.916
JH14-12	Blaik	34.56321	-97.50825	6620	2017.776
JH14-13	Blaik	34.56321	-97.50825	6700	2042.16
JH14-14	Blaik	34.56321	-97.50825	6825	2080.26
JH14-15	Blaik	34.56321	-97.50825	7050	2148.84
JH14-16	Blaik	34.56321	-97.50825	7125	2171.7
JH14-17	Blaik	34.56321	-97.50825	7275	2217.42
JH14-18	Blaik	34.56321	-97.50825	7375	2247.9
JH14-19	Blaik	34.56321	-97.50825	7575	2308.86
JH14-20	Blaik	34.56321	-97.50825	7725	2354.58
JH14-21 *	Whyte	34.53972	-97.41486	4800	1463.04
JH14-22 *	Whyte	34.53972	-97.41486	4850	1478.28
JH14-23	Whyte	34.53972	-97.41486	4915	1498.092
JH14-24	Whyte	34.53972	-97.41486	4960	1511.808
JH14-25	Whyte	34.53972	-97.41486	4990	1520.952
JH14-26	Whyte	34.53972	-97.41486	5030	1533.144
JH14-27	Whyte	34.53972	-97.41486	5085	1549.908
JH14-28	Whyte	34.53972	-97.41486	5125	1562.1
JH14-29	Whyte	34.53972	-97.41486	5155	1571.244
JH14-31	Whyte	34.53972	-97.41486	5910	1801.368
JH14-32	Whyte	34.53972	-97.41486	6110	1862.328
JH14-33	Whyte	34.53972	-97.41486	6130	1868.424
JH14-34	Whyte	34.53972	-97.41486	6175	1882.14
JH14-35	Whyte	34.53972	-97.41486	6230	1898.904
JH14-36	Whyte	34.53972	-97.41486	6260	1908.048
JH14-37	Whyte	34.53972	-97.41486	6310	1923.288
JH14-38	Whyte	34.53972	-97.41486	6360	1938.528
JH14-39	Whyte	34.53972	-97.41486	6410	1953.768
JH14-40	Whyte	34.53972	-97.41486	6450	1965.96
JH14-41	Whyte	34.53972	-97.41486	6485	1976.628

Appendix B - Major and Trace Element Geochemistry

Raw major and trace element geochemical analysis was performed using XRF at Franklin and Marshall College. Major element concentrations are provided in weight percent, while trace element concentrations are provided in parts per million. Samples were normalized to account for FeO and Fe_2O_3 from a total Fe_2O_3 (LeMaitre, 1976).

	JH14-11	JH14-12	JH14-13	JH14-14	JH14-15	JH14-16
SiO_2	52.41	57.88	53.71	50.27	53.85	50.53
TiO_2	3.29	2.60	3.11	3.21	2.90	3.14
Al_2O_3	12.70	12.78	12.90	13.44	13.21	13.34
Fe_2O_3	5.66	4.97	5.25	5.52	5.52	5.60
FeO	8.39	6.38	7.63	8.85	7.52	8.53
MnO	0.25	0.19	0.24	0.29	0.25	0.29
MgO	4.38	3.24	4.25	5.40	4.24	5.39
CaO	6.37	5.10	6.44	6.78	5.39	6.52
Na_2O	3.68	3.44	3.58	3.26	3.60	3.76
K_2O	1.50	2.34	1.61	1.53	2.23	1.49
P_2O_5	0.43	0.37	0.42	0.46	0.46	0.46
Total	100.00	100.00	100.00	100.00	100.00	100.00
LOI	2.63	2.55	3.10	3.81	2.60	2.84
Ba	331	501	371	545	515	481
Ce	25	41	28	30	36	29
Co	51	39	49	55	47	56
Cr	53	53	63	63	52	85
Cu	177	117	183	160	141	158
Ga	19.4	20.4	19.8	19.2	20.0	18.1
La	16	25	17	15	17	15
Nb	30.5	39.3	32.5	27.5	34.1	27.3
Ni	38	31	39	55	43	59
Pb	<1	10	8	<1	<1	<1
Rb	26.9	48.1	28.5	26.3	45.7	29.5
Sc	31	24	28	31	26	30
Sr	288	290	320	380	326	328
Th	9.8	4.8	7.3	3.4	9.0	1.1
U	0.5	0.8	0.7	<0.5	0.9	0.9
V	324	240	302	320	258	305
Y	43.2	49.5	44.7	39.7	45.2	38.0
Zn	148	156	147	150	141	139
Zr	302	400	326	246	320	217

	JH14-17	JH14-18	JH14-19	JH14-20	JH14-21	JH14-22
SiO_2	51.02	51.39	52.56	51.17	58.50	58.91
TiO_2	3.29	3.02	2.96	3.08	1.85	1.68
Al_2O_3	12.92	13.50	13.57	13.54	17.20	15.67
Fe_2O_3	5.74	5.63	5.52	5.56	4.71	4.76
FeO	8.68	8.35	7.90	8.22	5.65	5.46
MnO	0.26	0.28	0.25	0.27	0.10	0.12
MgO	4.70	5.38	4.74	5.23	3.35	3.41
CaO	6.73	5.76	5.68	6.08	1.40	2.36
Na_2O	3.33	3.51	3.80	3.72	1.05	1.81
K_2O	1.90	1.80	1.70	1.76	5.31	4.95
P_2O_5	0.46	0.46	0.43	0.45	0.25	0.26
Total	100.00	100.00	100.00	100.00	100.00	100.00
LOI	3.02	3.81	3.60	3.47	6.43	5.43
Ba	462	504	443	500	608	585
Ce	27	32	34	32	54	64
Co	51	54	49	55	39	37
Cr	67	69	78	74	80	81
Cu	184	138	145	150	113	138
Ga	19.4	19.0	19.8	18.6	25.0	22.1
La	15	13	17	16	26	32
Nb	29.5	27.5	29.8	29.2	60.0	53.1
Ni	46	60	53	58	61	56
Pb	10	10	<1	<1	6	<1
Rb	32.8	36.2	32.4	32.9	147.5	138.6
Sc	31	30	29	29	21	23
Sr	336	292	266	330	59	115
Th	2.4	7.8	3.2	2.0	21.3	10.9
U	<0.5	<0.5	<0.5	<0.5	1.3	<0.5
V	323	293	283	295	159	161
Y	39.5	39.5	40.7	38.5	58.8	58.3
Zn	152	146	145	139	194	205
Zr	273	226	274	231	466	430

	JH14-23	JH14-24	JH14-25	JH14-26	JH14-27	JH14-28
SiO_2	51.75	51.94	51.01	51.68	50.26	51.67
TiO_2	2.13	2.05	2.22	2.21	2.41	2.22
Al_2O_3	14.91	14.24	14.69	14.24	14.83	15.06
Fe_2O_3	5.29	5.08	5.30	5.16	5.33	5.06
FeO	7.41	7.42	7.90	7.68	8.10	7.31
MnO	0.20	0.21	0.21	0.21	0.20	0.20
MgO	6.55	6.49	7.07	6.80	6.95	6.60
CaO	4.74	6.02	5.02	5.56	5.30	5.17
Na_2O	3.44	3.66	4.02	3.94	4.41	3.64
K_2O	2.44	1.75	1.35	1.36	0.96	1.92
P_2O_5	0.31	0.30	0.32	0.29	0.34	0.33
Total	100.00	100.00	100.00	100.00	100.00	100.00
LOI	5.62	5.79	5.76	5.42	5.45	6.12
Ba	489	381	450	416	307	437
Ce	38	36	32	37	32	32
Co	55	57	63	61	61	57
Cr	91	72	73	80	89	169
Cu	166	164	150	174	167	159
Ga	18.1	16.8	17.9	17.1	17.7	18.3
La	17	13	14	12	12	13
Nb	31.2	26.1	27.7	27.5	28.0	30.0
Ni	64	64	68	67	74	70
Pb	7	1	7	13	9	7
Rb	49.1	27.6	18.7	17.4	12.5	33.9
Sc	32	34	37	35	37	34
Sr	238	244	266	203	203	211
Th	7.8	6.1	15.6	8.1	12.5	7.6
U	1.2	<0.5	0.6	<0.5	<0.5	<0.5
V	297	296	299	299	303	278
Y	38.7	37.1	36.6	35.2	34.1	37.4
Zn	168	147	178	181	179	165
Zr	217	180	177	175	174	199

	JH14-29	JH14-31	JH14-32	JH14-33	JH14-34	JH14-35
SiO_2	50.97	50.12	53.36	52.30	50.82	51.58
TiO_2	2.17	2.26	1.81	1.88	1.81	1.95
Al_2O_3	14.60	13.75	13.59	13.47	13.25	13.67
Fe_2O_3	5.08	5.02	5.94	6.02	5.42	5.29
FeO	7.64	7.91	7.86	8.41	8.77	8.04
MnO	0.21	0.22	0.20	0.25	0.04	0.21
MgO	6.84	6.21	4.30	4.50	4.96	5.05
CaO	6.02	8.40	5.56	6.10	9.11	7.93
Na_2O	3.87	4.21	3.87	3.63	2.90	3.28
K_2O	1.44	0.73	2.40	2.20	1.64	1.80
P_2O_5	0.31	0.30	0.25	0.29	0.30	0.30
Total	100.00	100.00	100.00	100.00	100.00	100.00
LOI	5.86	2.94	1.59	1.73	2.33	2.43
Ba	411	181	410	403	428	316
Ce	31	29	37	43	36	35
Co	58	59	57	56	55	53
Cr	133	132	56	45	36	38
Cu	153	158	162	145	145	166
Ga	17.1	15.6	17.0	16.8	15.1	15.6
La	13	14	17	19	17	18
Nb	26.8	24.2	23.4	22.6	20.2	22.8
Ni	68	69	50	48	47	49
Pb	<1	<1	<1	1	<1	2
Rb	21.5	11.4	55.8	41.8	39.5	37.3
Sc	36	39	35	37	9	37
Sr	263	432	269	244	241	375
Th	10.0	6.3	7.6	7.9	6.8	8.4
U	<0.5	<0.5	<0.5	0.7	<0.5	<0.5
V	344	359	345	285	259	373
Y	34.5	31.8	39.1	40.1	38.6	38.3
Zn	158	127	134	131	156	142
Zr	179	157	198	197	182	201

	JH14-36	JH14-37	JH14-38	JH14-39	JH14-40	JH14-41
SiO_2	52.88	52.86	53.92	54.60	55.74	54.95
TiO_2	1.82	1.76	1.78	1.69	1.65	1.69
Al_2O_3	13.44	13.18	13.47	13.11	13.28	13.16
Fe_2O_3	5.48	5.36	5.24	5.48	5.20	5.42
FeO	7.82	7.74	7.56	6.98	6.89	7.31
MnO	0.21	0.22	0.22	0.21	0.20	0.21
MgO	4.63	4.67	4.64	3.44	3.57	3.82
CaO	7.07	7.71	6.89	7.00	6.62	6.56
Na_2O	3.88	3.13	3.15	4.24	4.23	4.47
K_2O	1.59	2.20	1.98	2.15	1.52	1.28
P_2O_5	0.30	0.30	0.29	0.33	0.33	0.34
Total	100.00	100.00	100.00	100.00	100.00	100.00
LOI	1.72	1.62	1.61	0.89	1.15	1.41
Ba	554	543	436	545	464	412
Ce	41	42	43	60	52	52
Co	54	50	51	43	46	48
Cr	61	49	63	49	45	44
Cu	146	168	159	131	159	146
Ga	17.1	17.1	18.2	18.4	18.6	19.1
La	17	19	22	25	27	24
Nb	23.8	24.2	27.2	32.0	31.4	30.4
Ni	45	44	44	34	36	37
Pb	<1	<1	1	<1	<1	2
Rb	29.9	36.1	37.9	37.2	25.2	21.6
Sc	36	34	35	30	30	30
Sr	382	334	316	260	232	289
Th	8.8	8.7	6.5	9.8	6.2	7.7
U	<0.5	<0.5	<0.5	<0.5	<0.5	1.0
V	304	333	317	301	282	308
Y	43.4	43.2	45.2	49.5	49.2	48.1
Zn	131	129	137	124	131	129
Zr	226	231	252	304	299	270

Appendix C - Sr and Nd Isotope Analysis

Isotope analysis for Sr and Nd was performed by TIMS at the University of Kansas. The table below contains a complete list of measured and initial isotope ratios dated to 535 Ma, along with Rb, Sr, Sm, and Nd values in ppm for each of the seven samples analyzed.

	Rb	Sr	Nd	Sm	$^{87}Sr/^{86}Sr_m$	$^{87}Sr/^{86}Sr_i$	$^{143}Nd/^{144}Nd_m$	$^{143}Nd/^{144}Nd_i$	epsilon Nd
CB-PAW-1	25.3	382	22.8	4.96	0.706689	0.705296	0.512593	0.512131	3.2
CB-PAW-14	25.4	330	34.7	7.61	0.706848	0.705229	0.512513	0.512051	1.6
CB-PAN-8	27.7	328	46.19	9.57	0.706435	0.704660			
CB-PAN-16	52.2	370	59.1	12.05	0.707985	0.705014	0.512500	0.512063	1.8
CB-PAN-20	13	438	20	4.62	0.704593	0.703970	0.512647	0.512162	3.8
CB-PAJ-10	37.8	218	30	6.09	0.710066	0.706403	0.512525	0.512101	2.
CB-PAJ-13	28.6	292	29.3	6.18	0.707031	0.704971	0.512560	0.512129	3.1

Appendix D - Alteration Filter

The Arbuckle samples have undergone some low-grade metamorphism. Because of this, the alteration filter of Beswick and Soucie (1978) was used. Figure D1 shows major element ratios on a logarithmic scale. Unaltered samples should display a linear trend. Straying from this trend indicates significant alteration and those samples were removed from any interpretation in this thesis.

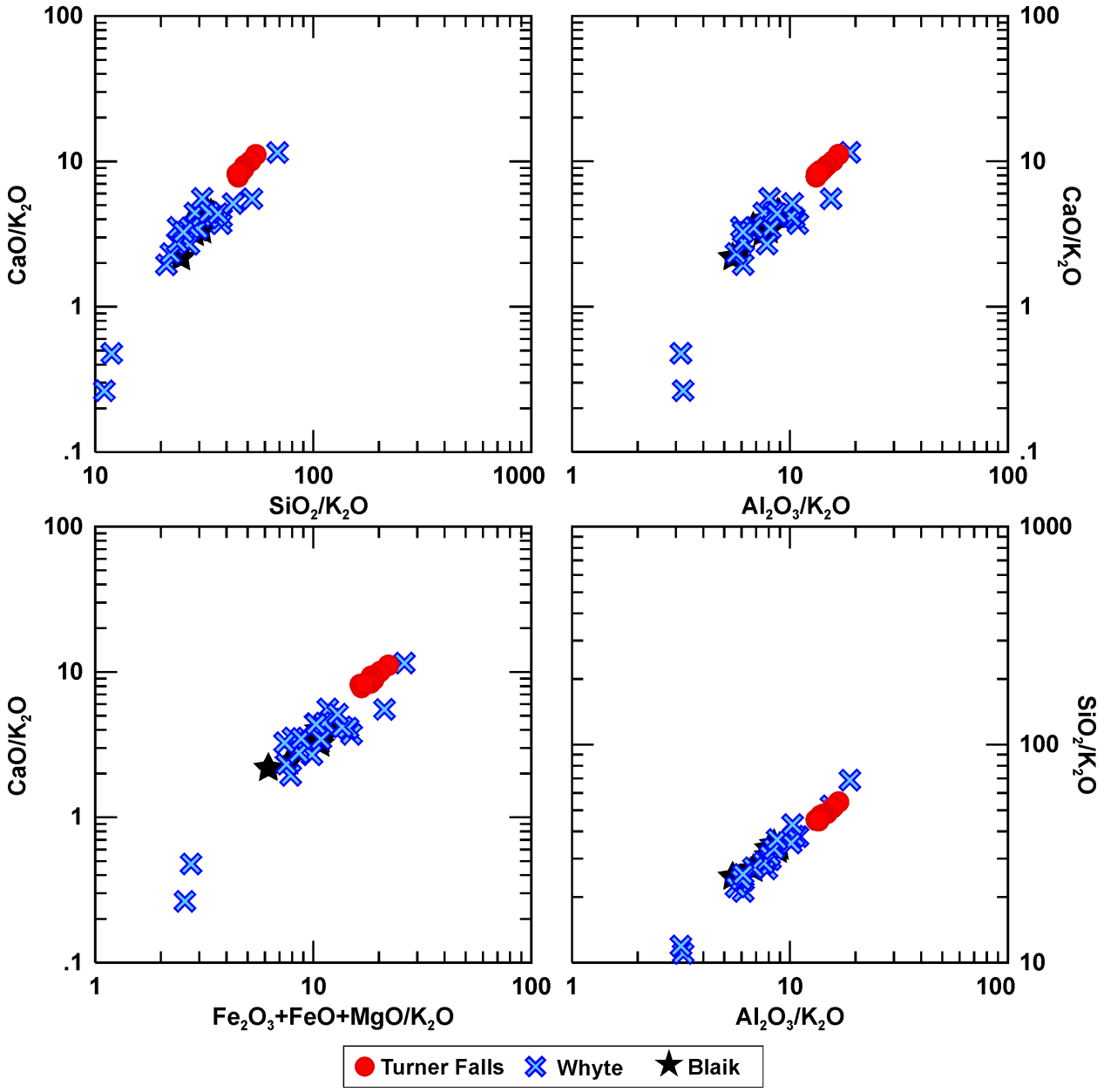

Figure D.1 Alteration filter" of Beswick and Soucie (1978) diagrams plotting molecular proportions of major element ratios.